
Development and characterization of a geostatic model for shallow CO₂ injection

Jessica M. Dongas and Don C. Lawton

ABSTRACT

A 25 sq. km static geomodel was updated for shallow injection into the 7 m thick Belly River Fm. at 295 m depth in Newell County, AB. Effective porosity and permeability were calibrated to six core lab analyses. A P10-50-90 framework was run to give conservative, typical, and optimistic scenarios of the reservoir's storage capacity. The regression shoreline sandstone interval remains consistent across the study area giving a mean effective porosity of 11% and permeability of 0.57 mD. Dynamic simulation was completed on the P10-50-90 static cases for multiple injection scenarios, totaling 5000 t/CO₂ after a 5-year period. No significant variations existed in the results between the three static cases. The evolution of the CO₂ plume was observed at 1-year during injection and 5-years during injection, as well as the 1-year and 10-year mark for the post-injection period. The final 10-year post-injection result simulated a laterally extensive plume, expanding to 350 m in length and 20 m of vertical migration above the BRS Formation. The target interval proves as an ideal reservoir, and the seal interval demonstrates containment over a 10-year post-injection period. Uncertainties remain in the static and dynamic realm, and include reservoir, fracture, and capillary pressure, k_v/k_h ratio, and the relative $k_{CO_2-H_2O}$. Further work is being completed on a 1 km x 1 km layer cake case, and will be used as documentation as a step towards obtaining the injection license as part of Directive 051 from the Alberta Energy Regulator.

Introduction

This study is based on the 5 km by 5 km geostatic model constructed in Dongas and Lawton (2014), and is a continuation to further update and characterize the BBRS Formation for shallow CO₂ injection. The injection zone is located in Newell County, AB at 295 m depth, and remains a consistent 8 m thickness throughout the geomodel. The structural grid is a combined input of interpreted formation tops on wireline data, and two 3-D seismic volumes. A time-depth relationship was established through three well ties, and velocity modeling enabled a depth conversion. The grid is comprised of vertical pillars representing the "layer-cake" geological setting of the Alberta prairies. The target and seal zones are layered and upscaled into cells 0.5 m in height. Using a Gaussian Random Function Simulation (GRFS) algorithm, the model is populated with effective porosity (PHIE) and intrinsic permeability (K_INT) using existing wireline data from 88 wells. The newly drilled injector well (10-22-17-16W4 or 10-22) provided measurements of six core analyses for porosity and permeability. The previous calculations used to calculate PHIE and K_INT have since been updated. This paper will discuss the static geomodel updated properties of PHIE and K_INT, the static P10-50-90 cases of the BBRS Formation, and the dynamic simulation results of injecting 1000 t/CO₂ for a five-year period. Further details regarding the construction of the model framework can be reviewed in Dongas and Lawton (2014).

Petrophysical Methods

Porosity – total and effective

Porosity and permeability are two of the most desirable variables required for reservoir characterization and dynamic fluid-flow simulation. There are different definitions of effective and total porosity. Total porosity is defined as the total void space in a rock, including both interconnected and isolated pore spaces along with the volume of immobile clay bound water (Schlumberger Oilfield Glossary, 2015). Effective porosity is defined as the interconnected pore spaces in a rock that enables fluid flow in a reservoir. There are two other definitions that will be used in this project when referring to effective porosity, known as PIGN and PIGE, calculated by Swager (2015) during the Elemental Log Analysis (ELAN). PIGN is defined as the total porosity without the volume of clay bound water, but includes capillary bound water. Whereas PIGE is defined as the connected pore spaces with the volume of capillary bound and clay bound water. These two effective porosity logs were computed only on the 10-22 well. (Swager, 2015)

The higher quality wireline and core data was only available in the 10-22 well, located at the center of the geostatic model. As for the remaining 87 wells, effective and total porosity were to be defined utilizing the minimal log suites available while remaining representative and comparable to the 10-22 data. As a result, total and effective porosity calculations were approached in a manner that considers the clay content, as well as the bound and free fluids. The approach is outlined below and was derived by Swager (2015).

First, the clay volume (*Volume_Clay*) is scaled (Eqn - 1) using the neutron-porosity (NPSS) and density-porosity (DPSS) logs. This is to scale the amount of clay content in the stratigraphic column, as very rarely is there 60-70% volume of clay in any shale formation.

$$Volume_Clay = 2.7(NPSS - DPSS) - 0.1 \quad (\text{Eqn - 1})$$

The volume of clay (VCL) is limited to 60-70% (Eqn - 2), defining the minimum of clay content to be 2% in any given rock formation in the stratigraphic column.

$$VCL = \max(0.02, \min(0.65, Volume_Clay)) \quad (\text{Eqn - 2})$$

Next, the total porosity (PHIT) is calculated using the NPSS and DPSS (Eqn - 3). Due to the high clay content in the Cretaceous stratigraphy, the NPSS log lead to calculating erroneously high total porosities. As a result, the DPSS log was much heavier weighted and is considered to be the most accurate and reliable log when borehole conditions are optimal (Rider and Kennedy, 2011).

$$PHIT = \left(\frac{0.1 * NPSS + 0.9 * DPSS}{1} \right) \quad (\text{Eqn - 3})$$

The volumes of free fluid (FF) and bound fluid (BF) are required to calculate the effective porosity, as well as to compute the permeability utilizing the Timur-Coates free fluid model (Luthi, 2013), which will be discussed in the next subsection. The BF is calculated by multiplying the VCL with a scalar *xx* that gives $PHIT \approx BF$ (Eqn - 4) in the

zone with the highest clay content. The zone of the highest clay content was determined by the maximum separation of the DPSS and the NPSS curves. The scalar multiplier typically lies within the range of 0.15 – 0.25 (Swager, 2015), where the best match of PHIT and VXBW was with the xx equal to 0.2 in the Pakowki Formation. The BF was then limited (Eqn - 5) to be only 0.003 less than PHIT. Lastly, the FF is defined by subtracting the BF from the PHIT shown in Equation 6.

$$VXBW = xx * VCL \quad (\text{Eqn - 4})$$

$$BF = \min(PHIT - 0.003, VXBW) \quad (\text{Eqn - 5})$$

$$FF = PHIT - BF \quad (\text{Eqn - 6})$$

When defined as the total pore spaces in the rock less the BF, the effective porosity (PHIE) is calculated in Equation 7,

$$PHIE = PHIT - BF \quad (\text{Eqn - 7})$$

It is typically found that the PHIE is lower than the PHIT in rock formations, as a result of not including the isolated voids and respective fluids in the calculations. However, the PHIE and PHIT both gave erroneously high values for the coal zones in the Foremost Formation, with porosities greater than 30%. The coal zones typically have a matrix density of 1.2 g/cc, which is much lower than the typical 2.65 g/cc value of a sandstone (Rider and Kennedy, 2011). As a consequence of this approach, facies modeling served as a method to identify, isolate, and re-assign reasonable porosity values based on numerous wireline cut-offs.

Through observation, the PHIT values in the coal zones within the Foremost Formation exceeded 30% and appeared to be the highest porosity values in the stratigraphic column. The coal zones are known to have methane gas (CH₄) and are water-saturated (Pedersen, 2014). Thus to limit the coals with the assumption of low relative permeability (Eqn - 8), it is shown that

$$PHIT = \text{if}(PHIT > 0.3, 0.03, PHIT), \quad (\text{Eqn - 8})$$

the coal beds are assumed to have 3% PHIT, relative to the other free and bound water and gas present in these zones.

Other lithologies that read values of 20% were deemed reasonable, but were also considered to be on the higher-end of the PHIT. Another challenge was found in negative PHIT values, where the BF must have exceeded the PHIT in order to compute a negative value. To mitigate and limit negative and erroneously high PHIT values, Equations 9 and 10 display the syntax used,

$$PHIT = \text{if}(PHIT > 0.2, 0.2, PHIT) \quad (\text{Eqn - 9})$$

$$PHIT = \text{if}(PHIT < 0, 0.001, PHIT) \quad (\text{Eqn - 10})$$

where any values of PHIT greater than 20% remain at 20% and similarly any negative values of PHIT are eliminated and are re-assigned to a near-zero value.

For calculating the facies model, a simple lithology legend was used to only discriminate between coal, sandstone, silty-sand, and shale formations. Based on the limited logs available, the lithology model cannot be complex. The characterization could be improved by careful QC of each log and repaired where possible, however this adds cost. The different facies are identified through a numerical code such that coal (1), sand (0), silty-sand (2), and shale (3) are written as their respective number in the following equations. To identify coal zones within the Foremost Formation, the bulk density (RHOB), compressional sonic (DT), NPSS, GR, and PHIT logs are used. Coal zones generally have a bulk density less than 2 g/cc, have characteristically higher NPSS values greater than 44%, and appear to have a fast transit time measurements greater than 130 μ s/ft (Rider and Kennedy, 2011). To limit the porosity of the coal zones, the following Equations 11 - 18 demonstrate the identification of the coals and other lithologies whilst using the facies numerical coding.

$$FACIES = if(RHOB < 2, 1, FACIES) \quad (\text{Eqn - 11})$$

$$FACIES = if(NPSS > 0.44, 1, FACIES) \quad (\text{Eqn - 12})$$

$$FACIES = if(FACIES = 1, 1, if(GR < 50, 0, FACIES)) \quad (\text{Eqn - 13})$$

$$FACIES = if(FACIES = 1, 1, if(GR > 95, 3, FACIES)) \quad (\text{Eqn - 14})$$

$$FACIES = if(FACIES = 1, 1, if(GR > 50, if(GR > 95, 2, FACIES), FACIES)) \quad (\text{Eqn - 15})$$

$$FACIES = if(DT > 130, 1, FACIES) \quad (\text{Eqn - 16})$$

$$FACIES = if(PHIT > 0.3, 1, FACIES) \quad (\text{Eqn - 17})$$

$$FACIES = if(PHIT = 0.03, 1, FACIES) \quad (\text{Eqn - 18})$$

Aside from the wireline data that have computed effective and total porosity logs, there was a total of three core points within the BBRS Formation from the 10-22 well. Three core samples measured for total porosity using the Routine Core Analysis (RCA), and the same core samples measured for total and effective porosity using the Tight Rock Analysis (TRA) completed by Schlumberger Reservoir Laboratories Canada (2015).

The RCA method involved humidity drying the core in 40% relative humidity conditions in an oven at 60°C until the weights are stabilized. The Helium porosity is measured using the CoreTest AP-608, a porosimeter-permeameter, and is based on the unsteady-state pressure fall-off method at confining pressures of 800 pounds per square inch (psi). (Schlumberger Reservoir Laboratories Canada, 2015)

The TRA method is a retort analysis of the core samples, and is performed on core biscuit samples. The porosity is calculated from a crushed portion of the core plug that is chosen to be representative of the sample. Once the chosen portion is crushed and sieved to the proper grain size, the sample is weighed and heated in a retort vessel to an initial temperature. The initial temperature stage acts to drive off the interstitial water, however once the water has been driven off, the vessel temperature is increased as a final effort to remove any remaining fluids. (Schlumberger Reservoir Laboratories Canada, 2015)

The core measurement results from both the RCA and TRA methods can be seen in Table 1. The effective and total porosity values at these specific depths within the BBRS Formation were included in the porosity interpretation and estimation of the target interval.

Table 1. The core measurement results from the RCA and TRA methods provided by Schlumberger Reservoir Laboratories Canada (2015).

Sample	Depth (m)	Tight Rock Analysis		Routine Core Analysis
		Total Porosity (%)	Effective Porosity (%)	Helium Porosity (%)
2	297.15	-	-	9.2
3	298.93	-	-	13.5
4	300.08	-	-	12.2
W4-2	294.37	16.87	10.11	

In comparison to the calculations completed on the wireline data for the total 88 wells, the effective porosity values in the BBRS Formation were an order of magnitude lower. The calculated effective porosity had a mean value of approximately 4%, and required PHIE to be recalculated with a new volume of BF. Once the core measurements were plotted against the wireline data, the PIGN effective porosity calculated during the ELAN for 10-22 appeared to match the porosity measurements given by the core analyses. As a result, the PIGN effective porosity was set to remain as the PHIE log for the 10-22 well and the remaining 87 wells were recalculated (Eqn - 19) using a scalar multiplier xx of 0.13 (Zaluski, 2015), where

$$BF2 = xx * VCL. \quad (\text{Eqn - 19})$$

The PHIE (Eqn - 20) was recalculated, subtracting the new bound fluid (BF2) from the original PHIT,

$$PHIE = PHIT - BF2, \quad (\text{Eqn - 20})$$

which achieved the goal of producing a comparable log curve to the PIGN in the 10-22 well. The estimated mean effective porosity in the BBRS Formation is 11%, which is comparable and within range of the core lab measurements. Figure 1 demonstrates the PIGN effective porosity plotted against the calculated PHIE and core lab measurement points.

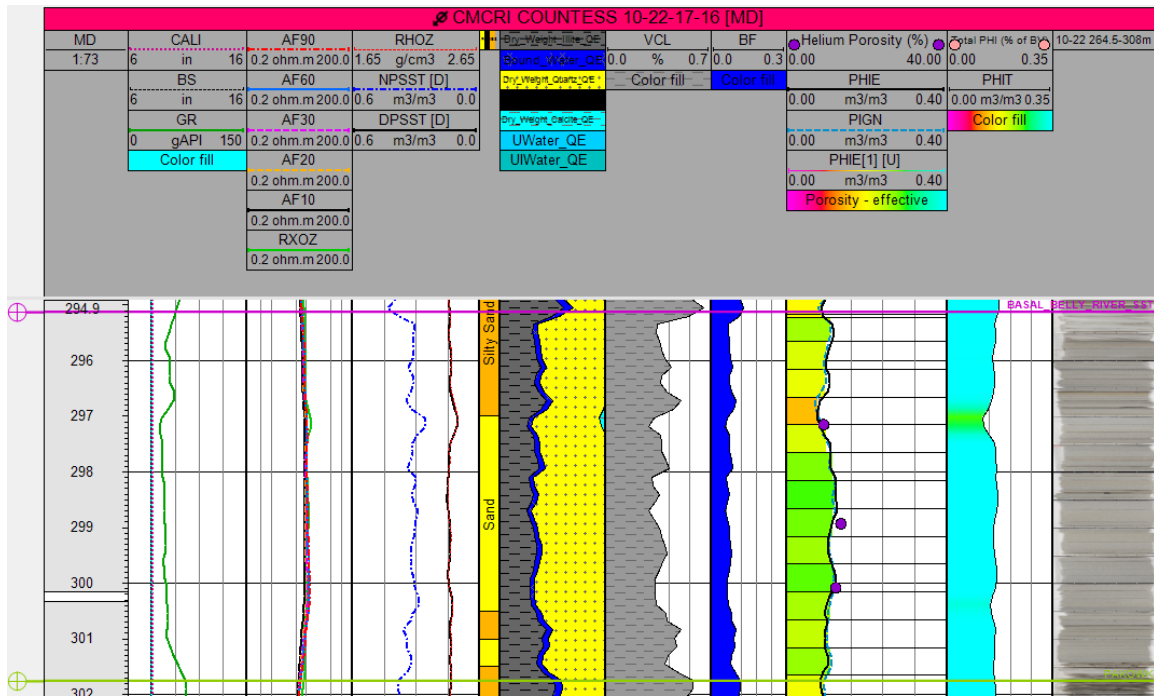


FIG 1. Well section window of the 10-22 well displaying the PIGN, PHIE, and the core lab measurement points within the BBRs Formation. The top and bottom of the BBRs Formation is marked by the pink and green horizontal marker, respectively.

In comparison to the Peco and Pembina Fields, where the BBRs Formation is producing, the average porosity value for both fields is 8.5% (Meurant, 2011; Gardiner et al., 1990). Porosity values said to be typical of this Formation range from 10-24%, averaging 18% in the Plains (Hamblin and Abrahamson, 1993). The calculated effective porosity values from the wireline data and the core lab measurements from the TRA and RCA analyses lie within these ranges. Gardiner et al. (1990) identified differences between the porosity measurements amongst the core and the wireline data to be attributed to authigenic clays. The authigenic clays are known to limit permeability at reservoir conditions at depth, but have the tendency to shrink whilst air-dried in the core samples leading to overestimated porosity measurements (Gardiner et. Al, 1990; Swager, 2015).

Permeability

Permeability (k) as a rock property is dependent on the structural organization of individual grains such as compaction, grain sorting, pore geometry, pore connectivity, as well as tortuosity. Mineralogy and grain size also affect permeability, especially when clay minerals are present. Clay minerals act to reduce permeability by clogging pore throats, where “kaolinite is less harmful than illite, which is less harmful than smectite” (Herron, 1987). Permeability is generally heterogeneous and anisotropic, where vertical permeability (k_v) is typically lower in laminated beds than horizontal permeability (k_h). In addition to a rock property, permeability also acts as a fluid property. The permeability is also dependent on whether the fluid type is compressible or incompressible, whether tortuosity promotes laminar or turbulent flow, and lastly, if there are multiple fluid phases the relative permeability will be subject to change. (Meyers, 2014)

From the wireline data available and the core lab measurements from the 10-22 well, primary intrinsic permeability was estimated on a meso to macro scale (Meyers, 2014). The measurements from the core lab indicated secondary permeability from vertical and horizontal fractures within the core plugs, however these were not taken into consideration for modeling. For future recommendation, primary permeability, secondary permeability, as well as the k_v/k_h ratio should be incorporated into the geological model to enhance fluid-flow reservoir simulation results.

Following the free and bound fluid approach in calculating the effective porosity, intrinsic permeability (K_{INT}) was approximated using an equation based off of the previous work of Timur (1968) and Coates and Dumanoir (1974). Equation 21 is known as the Timur-Coates free-fluid model, and calculates permeability (K_{TIM})

$$K_{TIM} = a\phi^m \left(\frac{FFV}{BFV} \right)^n, \quad (\text{Eqn - 21})$$

where ϕ is the total porosity and involves the ratio of free-fluid volume to bound-fluid volume. The variables a , m , and n are commonly 10^4 , 4, and 2, respectively (Allen et al., 2000). Utilizing Equation 22 with our syntax, the equation becomes

$$K_{INT} = 1000(PHIT)^4 \left(\frac{FF}{BF} \right)^2, \quad (\text{Eqn - 22})$$

where variables m and n remain at 4 and 2, respectively, and a has been modified to 10^3 . Due to the limited wireline data in the 87 wells, CMR data was not used, however it is recommended if present to utilize CMR data to improve the porosity-permeability relationship with better FF and BF measurements. The K_{INT} log produced reasonable values along the full stratigraphic column, however the coal zones proceeded to act erroneously with the high PHIT values. Amongst the other lithologies, it appeared that the permeability did not estimate greater than 3 mD. To limit the coal permeability, Equation 23 demonstrates that if the wireline data detects a coal,

$$K_{INT} = \text{if}(FACIES = 1, 0.001, K_{INT}), \quad (\text{Eqn - 23})$$

to limit the K_{INT} to 0.001 mD. With the presence of water and CH_4 gas, it was assumed that the relative permeability was very low and non-zero. Furthermore, where permeability values did not exist (NAN), another permeability (K_{INT_GEO}) was substituted. The K_{INT_GEO} is a permeability calculated in the ELAN dataset for the 10-22 well utilizing the Herron (1987) method. This method uses a “porosity and mineralogy model where each mineral in the ELAN model has a permeability factor” (Swager, 2015). The substitution using K_{INT_GEO} is seen in Equation 24 as

$$K_{INT} = \text{if}(K_{INT} = \text{NAN}, K_{INT_GEO}, K_{INT}). \quad (\text{Eqn - 24})$$

In addition to the porosity measurements discussed in the previous subsection, permeability was another parameter measured on the three core plugs within the BBRS Formation. Three core samples measured for total porosity using the Routine Core Analysis (RCA), and the same core samples were measured for total and effective porosity using the Tight Rock Analysis (TRA) completed by Schlumberger Reservoir Laboratories Canada.

The RCA method involved humidity drying the core in 40% relative humidity conditions in an oven at 60°C until the weights are stabilized. Nitrogen permeability was measured using the CoreTest AP-608 porosimeter-permeameter. The unsteady-state pressure fall-off method was used and set at a confining pressure of 800 psi, identical to the measurement process of collecting the helium porosity data. The core sample is then exposed to a high-pressured nitrogen gas (N₂) source released upstream, and the sample is monitored as the N₂ gas flows through the sample. The rate at which the pressure flowing through the sample reaches equilibrium with the downstream pressure is used to determine permeability (Nolen-Hoeksema, 2014). Nitrogen gas is generally preferred than air or helium (He) because it is an inert gas. Permeability that takes into account the Klinkenberg effect is known as the Klinkenberg permeability. The Klinkenberg effect is due to the slip flow of gas that occurs at the pore walls, and acts to enhance the gas flow rate when the pore sizes are very small due to the greater larger surface area available (Tanikawa and Shimamoto, 2006). Typically, gas permeability is larger than water permeability, and water permeability can be calculated from gas permeability provided the Klinkenberg correction is applied (Tanikawa and Shimamoto, 2006). Nitrogen gas is also chosen when measuring Klinkenberg permeability, because the gas slippage is less pronounced in comparison to Helium and air (Rushing et al., 2004). The measurements are quality controlled by using a check plug made of stainless steel of known permeability similar to the core plug permeability, and is checked every fifth core plug. (Schlumberger Reservoir Laboratories Canada, 2015)

The TRA method measured the pressure-decay matrix permeability on a specific weight fraction of the crushed and sieved sample at saturation conditions. Saturation conditions of a core plug are determined prior to further core analyses. The pressure-decay permeability is then defined as the permeability to gas, and is derived from data collected from a gas expansion measurement. This method suggests by crushing the core sample, it removes artifacts from the rock and provides greater access to pore spaces to provide greater data accuracy – especially in mudstones and shales. (Schlumberger Reservoir Laboratories Canada, 2015)

The core measurement results from both the RCA and TRA methods can be seen in Table 2. The intrinsic permeability values at these specific depths within the BBRS Formation were included in the permeability interpretation and estimation of the target interval.

Table 2. The core measurement results from the RCA and TRA methods provided by Schlumberger Reservoir Laboratories Canada (2015).

Sample	Depth (m)	Tight Rock Analysis		Routine Core Analysis
		Nitrogen k (mD)	Klinkenberg k (mD)	Pressure-Decay k (mD)
2	297.15	0.466	0.365	
3	298.93	0.390	0.183	
4	300.08	1.21	0.738	
W4-2	294.37	-	-	0.000038

Sample W4-2 was interpreted to have too great of permeability to be accurately measured by the pressure-decay method. This sample was concluded to have reasonable total and effective porosities measured with this method, however the very low permeability are suggested the core sample has higher complexity that is beyond this method of measurement. In comparison to the other permeability values measured on a full core plug samples, as well as the permeability estimated using the Timur-Coates equations, sample W4-2 demonstrates very low and erroneous permeability.

The majority of estimated permeability readings over the full stratigraphic column in the 10-22 well are less than 3 mD, other than the coal zones in the Foremost Formation which were re-assigned to 0.001 mD. From the core lab analyses, the permeability results are observed to generally occur below 1 mD. In order to honour the core lab analyses and scale back the estimated K_{INT} log (Eqn - 25),

$$K_{INT} = \text{if}(K_{INT} > 3, 3, K_{INT}), \quad (\text{Eqn - 25})$$

where any values greater than 3 mD are set to remain at 3 mD. As well, any estimated K_{INT} values greater than 1 mD were scaled down by a factor of 0.25 (Eqn - 26),

$$K_{INT} = \text{if}(K_{INT} > 1, K_{INT} * 0.25, K_{INT}), \quad (\text{Eqn - 26})$$

in order to have the K_{INT} log tracing over the plotted core points in the 10-22 well. The mean estimated intrinsic permeability in the BBRs Formation is 0.57 mD, which is comparable and within range of the core lab measurements. The calcite cement matrix in the BBRs Formation appears to be limiting the primary intrinsic permeability, which could possibly contribute to the lower range of estimated permeability. Figure 2 displays the well section window of the 10-22 well with the Timur-Coates estimated permeability, with the three core measurements plotted to demonstrate how well the core and wireline data correspond with each other.

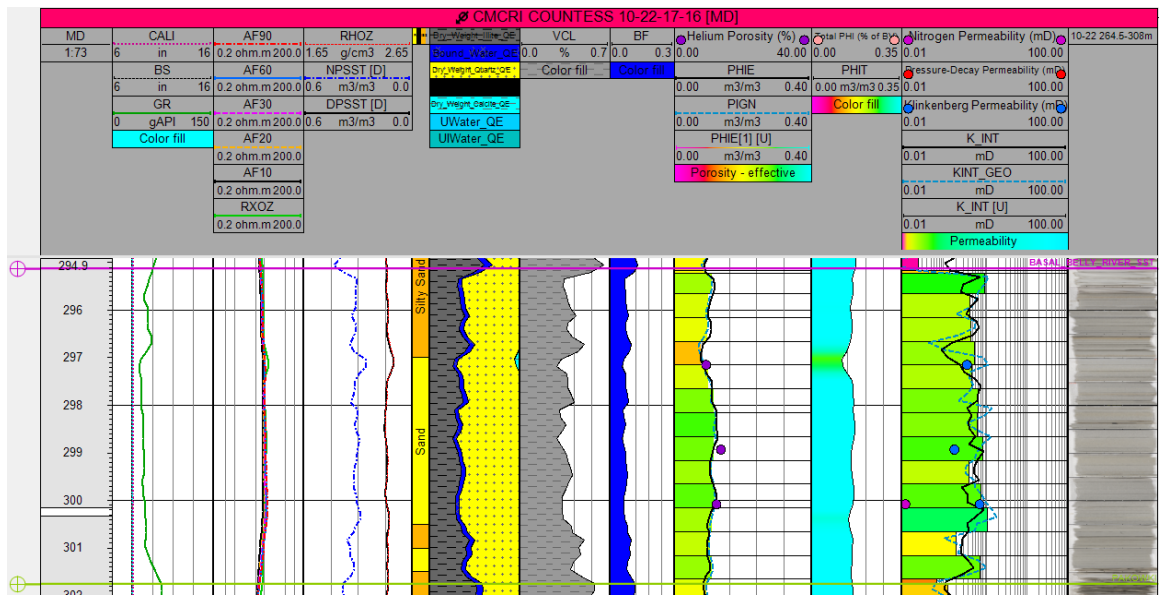


FIG 2. Well section window of 10-22 well displaying the permeability estimated using the Timur-Coates equation, and the plotted core lab measurements to display how well the data is integrated.

It is known that these Late Cretaceous sediments have not been buried to a great depth, and many of them remain unconsolidated with high pore-water volumes (Pedersen, 2014). The presence of the coal zones in the Foremost Formation demonstrated challenges while estimating the effective porosity and intrinsic permeability. Caution was taken through the re-assignment of lower total porosity and intrinsic permeability values, as less dense coals can be very porous but can act as impermeable barriers limiting vertical mobility of pore fluids and gases. Coal permeability is often determined by cleats, which are sets of joints that are perpendicular to the top and bottom of the coal seam where two sets of cleats develop an orthogonal pattern (Thomas, 2002). Cleats are natural fractures in coals, and act as conduits for the flow of fluids and gases. Numerical information of the coal zones within the Foremost Formation are not available at present in the public domain (Beaton, 2003), but through observation of the core samples in the 10-22 well, the coals did not demonstrate any fractures or cleat networks.

Aside from coal zones, increasing effective porosity typically gives increased permeability. Figure 3 shows this trend from the estimated effective porosity and intrinsic permeability in the geostatic model. This is generally true in clastic sediments, however secondary porosity can occur at depth with increasing temperatures due to the geothermal gradient. Carbonate sediments have greater complexity due to the geochemical alteration and greater heterogeneity when describing secondary porosity, thus this trend is typically not applied to carbonate formations. (Meyers, 2014)

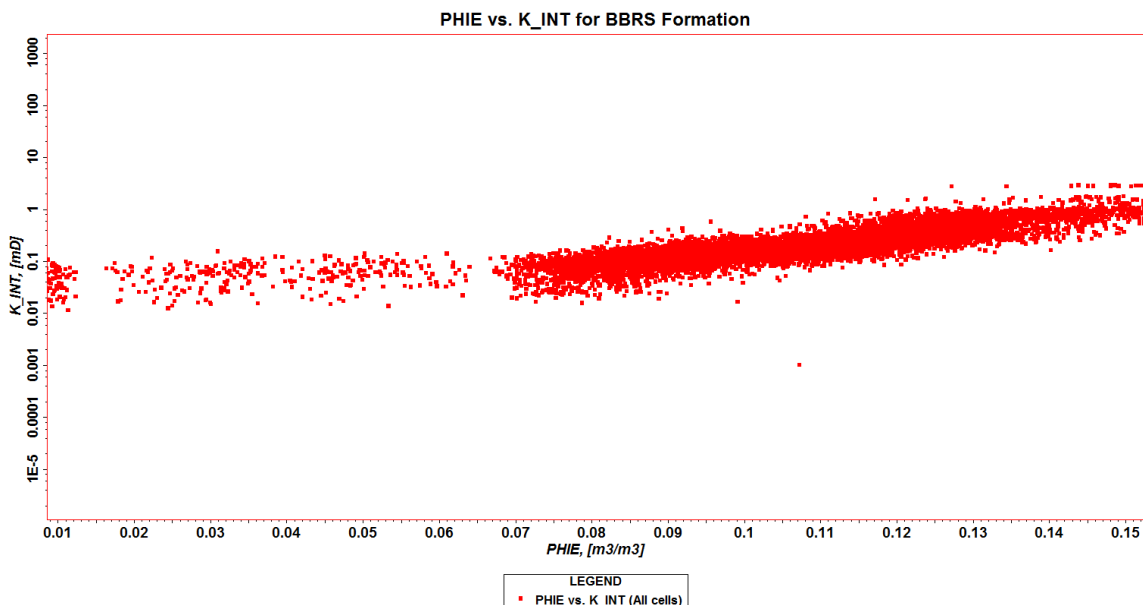


FIG 3. Porosity-permeability relationship between PHIE and K_INT for the BBRs Formation.

From other producing oil and gas fields located within Alberta, the shoreface-related sandstone typical of the BBRs Formation is known to have an average of 8 mD in the Plains (Hamblin and Abrahamson, 1993). Looking at specific fields such as the Pembina Field, the BBRs Formation has been described to have fair permeability ranging from 1-15 mD (Meurant, 2011). Another study (Gardiner et al., 1990) plotted 47 core points of porosity and permeability, fitting a least-squares-fit straight line that indicated a core porosity of 8.5% to have permeability of 1 mD. In comparison to these producing fields, the porosity-permeability relationship leans towards the lower end of fair to low permeability. This and the lack of hydrocarbons present is most likely the reason why the BBRs Formation is not producing in this area.

Log-to-core calibration

Log-to-Core calibration aims to correlate the core permeability with the calculated well log intrinsic permeability, as downhole tools cannot directly measure this important reservoir parameter. The vertical resolution differs between core plug measurements and a well log. Core plugs are discontinuous in nature, and specific locations are chosen within a reservoir and seal for laboratory analyses. Well logs are continuous in nature, and typically have a vertical resolution of 30-45 centimeters (cm) with measurements dependable on borehole conditions (Swager, 2015). Effects from bulk compressibility and handling may contribute to poor or inaccurate laboratory analyses (Swager, 2015). In this case, few core plugs fell apart during cleaning and were considered unsuitable for the laboratory RCA tests and not included in further analyses (Schlumberger Core Lab Canada, 2015).

Calibration of wireline logs with available core data in a well enhances reservoir characterization by increasing data density and improving the geological and geophysical interpretation in the formation of interest. In this dataset, only the 10-22 well has core data

available with porosity and permeability measurements completed and was used for log-to-core calibration.

The total and effective porosity measurements from the three core points located within the BBRS target interval were compared to the estimated wireline logs. The wireline PHIT log was calculated using a weighted average of both the NPSS and DPSS, and was comparable to the Helium Porosity measurements completed in the RCA. Calibrating the core porosity is required when relying solely on density and neutron log data, where the matrix density is unknown (Swager, 2015). Thus, the PHIT log did not require calibration with the core total porosity measurements.

The PHIE log was calculated based on an approach that involved estimating the volumes of clay present, the bound fluid, and the free fluid derived by Swager (2015). Originally, the PHIE log overestimated the amount of BF, producing a suppressed estimation of PHIE for the entire stratigraphic column. A second iteration of PHIE was calculated using a lower amount of BF, which produced a similar log response as the calculated PIGN curve during the ELAN. This second iteration of PHIE and the PIGN curve are comparable to the effective porosity measurements completed through the retort analyses in the TRA. A comparison with the CMR curve was also made between the core measurements and the calculated PHIE curve, which followed and agreed with the PHIE values (Swager, 2015). As a result, the PHIE or PIGN logs did not require calibration with the core effective porosity measurements. However, the availability of the core measurements proved to be an invaluable tool to compare values of both total and effective porosity in the target interval.

The permeability measurement from the identical three core points located within the BBRS target interval were compared to the estimated intrinsic permeability log, calculated using the Timur-Coates equation (Luthi, 2013). The estimated intrinsic permeability log read values too tight for the first iteration of PHIE, and again similar to the effective porosity issue. With the second iteration of PHIE, which resulted in producing a PHIE log similar to the PIGN log, the K_INT curve increased. A first pass of correlating the KINT_GEO from the ELAN dataset to the calculated K_INT was completed for the entire length of the 10-22 well. However, the K_INT curve required a calibration step in order to honour the core-measured permeability in the BBRS Formation. The K_INT curve was re-adjusted and increased using a 10:1 scalar factor, as matching the target permeability was of highest priority (Swager, 2015). The difference between the non-calibrated and the calibrated K_INT curve, along with the plotted core points is shown in Figure 4.

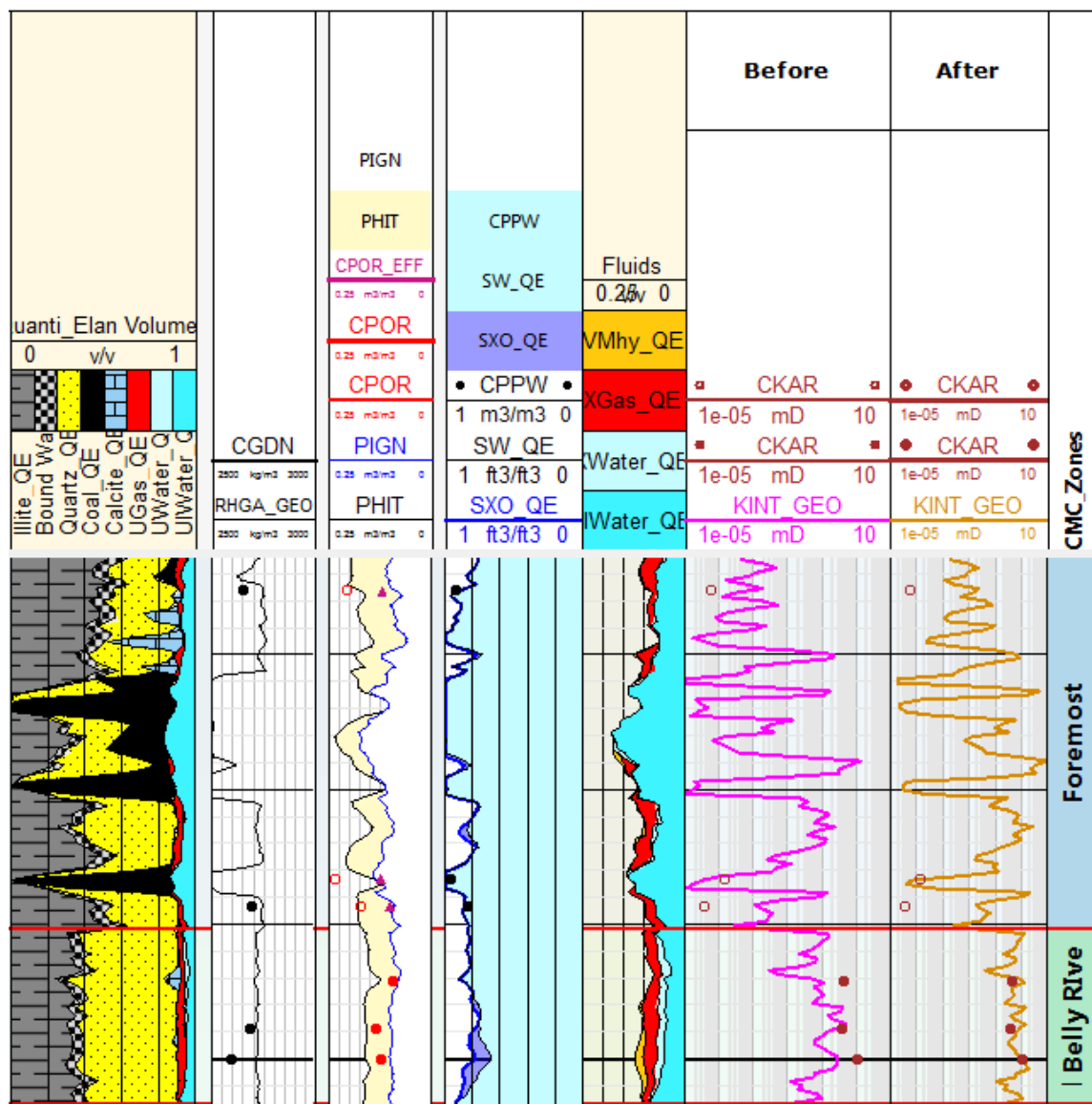


FIG 4. Before and after log-to-core calibration of K_INT data for the 10-22 injector well, from Swager (2015).

It is not unusual for the calculated permeability to require calibration. It is known that the NMR downhole tool produces fairly accurate measurements, however, small pore radii can mislead the tool to incorrectly measuring the cut-off for bound fluids (Swager, 2015). Often lab analysts and petrophysicists calibrate two parameters that affect the NMR logs, which include the time cut-offs for bound fluid (T2) and permeability modeling coefficients (Oxford Instruments Industrial Analysis, 2014).

The importance of obtaining core measurements is critical as a means of quality control and calibration. There can be differences with orders of magnitude between measured and estimated values, originating from the presence of micro-fractures, large authigenic clay volumes, as well as relative permeability effects if all parameters are not considered (Petrowiki, 2015). Without core measurements, porosity and permeability may be under-

reported and can lead to imprecise representations or misinterpretation of a reservoir (Oxford Instruments Industrial Analysis, 2014).

Model Uncertainty

Sources of uncertainty in static geological models

Models are tools to approximate reality and can be conceptual, mathematical, or a combination of the two (Meunier et al., 2013). In part of risk assessment and management, geological reservoir modeling is a vehicle used to highlight these risks and quantify uncertainty (Fichtl et al., 2013; Bentley, 2013). Understanding the sources of uncertainty and the associated risks aid in decision-making processes for the development, exploration, and production of a target interval.

The modern-day advancements in technology have supported the increase in size of geological and simulation models. Often the number of realizations iterated by these models aids in expressing and defining the uncertainty in the data, where higher number of realizations is preferred. The common size and complexity of geological models have become great, to which the handling capability of both the software and hardware are being challenged. The quality and accuracy of a geomodel should not be defined by its size or complexity, as best practices of geomodeling are continuously redefined with the technology advancements. (Bentley, 2013; Stunell, 2013)

Sources of uncertainty are scattered throughout the modeling process, from the data input to the a priori geological knowledge, assumptions, and thought processes of the geomodeller. Sources of uncertainty can be static or dynamic, where the latter is associated with fluid-flow simulations and is typically analyzed by a reservoir engineer. Data quality is a major source of uncertainty, and has led to poor reservoir performance predictions (Fichtl et al., 2013). Skorstad and Leahy (2013) state truthfully that it is a mistake to consider acquired field data to be 100% accurate, whether the data be wireline logs, seismic reflection data, or core measurements. The lack of precise data or well control (wireline and core data) increases static uncertainty, as these data inputs provide excellent but finite deterministic control on both stratigraphic and depositional model frameworks (Cox et al., 2013; Meunier et al., 2013). When considering wellbore position and associated uncertainty, understanding the well path and drilled trajectory is critical. In addition to the subsurface position and location of the wellbore, uncertainty lies in the assumption that wireline logging tools are calibrated and used with standardized QC operating procedures (Skinner, 2013). Best Practices of wireline logging may not always be performed and can lead to poor borehole measurements. An example includes lowering logging tools too quickly, leading to poor borehole conditions or mismatched depth-to-log measurements that require post-processing QC.

The lack of imprecise data such as seismic reflection data can also increase static uncertainty. A common pitfall to geomodellers is to assume the seismic data is solely sufficient in producing a structural model (Skorstad and Leahy, 2013). Although seismic data provides constraints on a larger scale for gross structural and stratigraphic frameworks, the understanding of a depositional framework is poorly defined without the refinement of well data (Cox et al., 2013). Höcker (2013) noted that uncertainties associated with subsurface depth and structures have the longest track record of applying stochastic

methods to quantify uncertainty. Velocity modeling for model depth conversion is also defined as a source of uncertainty. The quality of the seismic volume affects the horizon picking uncertainty, which affects the TWT input for computing interval velocity. The quality of the sonic logs and access to check-shot data affects the quality and validity of a well-to-seismic tie. Estimated interval velocities can be erroneous with stretch-squeeze adjustments, which results in affecting the TDR as seen in this GFRS model. Integration of velocity information can be useful for estimating realistic ranges. However, velocity models with high complexity or velocities conflicting with geomechanical and lithological trends can produce velocity-related depth errors (Höcker, 2013).

Combining the knowledge of known static and dynamic sources of uncertainty can raise the awareness of the geomodeller, affecting the workflows used through the duration of model construction. Geological and geophysical interpretation can be completed with greater understanding and knowledge of datasets if uncertainties are exposed and highlighted (Bond, 2013). The predication capability of the geomodel may be limited by unknown sources of uncertainty, which cannot be accounted for (Meunier et al., 2013). If constructing a model in a previously developed field, history matching of data and uncertainty analyses can be utilized as a basis for geological knowledge and comparison. Increasing data density and integrating multiple data sets, reduces the risk of producing radical errors in a geomodel (Meunier et al., 2013). Communication of uncertainty amongst industry professionals in the field to the boardroom is critical when advancing the development of the model, and making business decisions based on the results produced by a static or dynamic geomodel.

For this geostatic model, a P10-50-90 framework was used to quantify the uncertainty. This method produces equi-probable outcomes of the effective porosity and intrinsic permeability over a number of realizations, and analyzed for the total pore volume distribution.

P10-50-90 Statistic Analyses

As described by Mao-Jones (2012), “uncertainty should be modeled with probability distributions (a range of possibilities combined with probabilities assigned to each of those possibilities).” In order to communicate the uncertainty that is within the property model, the P10-50-90 framework was used. It refers to the data ranges between the 10th, 50th, and 90th percentiles. The P10 is typically referred to as the conservative outlook or the “lowest value that the expert thinks that the uncertain variable could be” (Mao-Jones, 2012). The P50 is typically referred to as the typical or “most likely value” (Mao-Jones, 2012). Lastly, the P90 is often referred to as the most optimistic, or the “highest values that the expert thinks the variable could be” (Mao-Jones, 2012). Any data points that lie before the P10 and after the P90 are very unlikely scenarios (Zaluski, 2014).

As a result of constructing a geomodel with over 60 million 3-D cells, a 1 km x 1 km volume clip of the BBRs Formation centered at the main 10-22 well was used. The base of the Foremost Formation and the top of the Pakowki Formation defines the vertical extent of the volume clip. A workflow was constructed to model the PHIE for 40 iterations. Due to the capacity of computation power, there was a limitation on the number of iterations that could have been run. It is understood that the greater number of model iterations will

produce a data distribution closer to a normal score. As well, the static uncertainty is better defined with a large number of model realizations. Once the total effective pore volumes were modeled, a total of 22 bins were used to organize the data by frequency and range and plotted to view the distribution for the BBRs Formation (Figure 5).

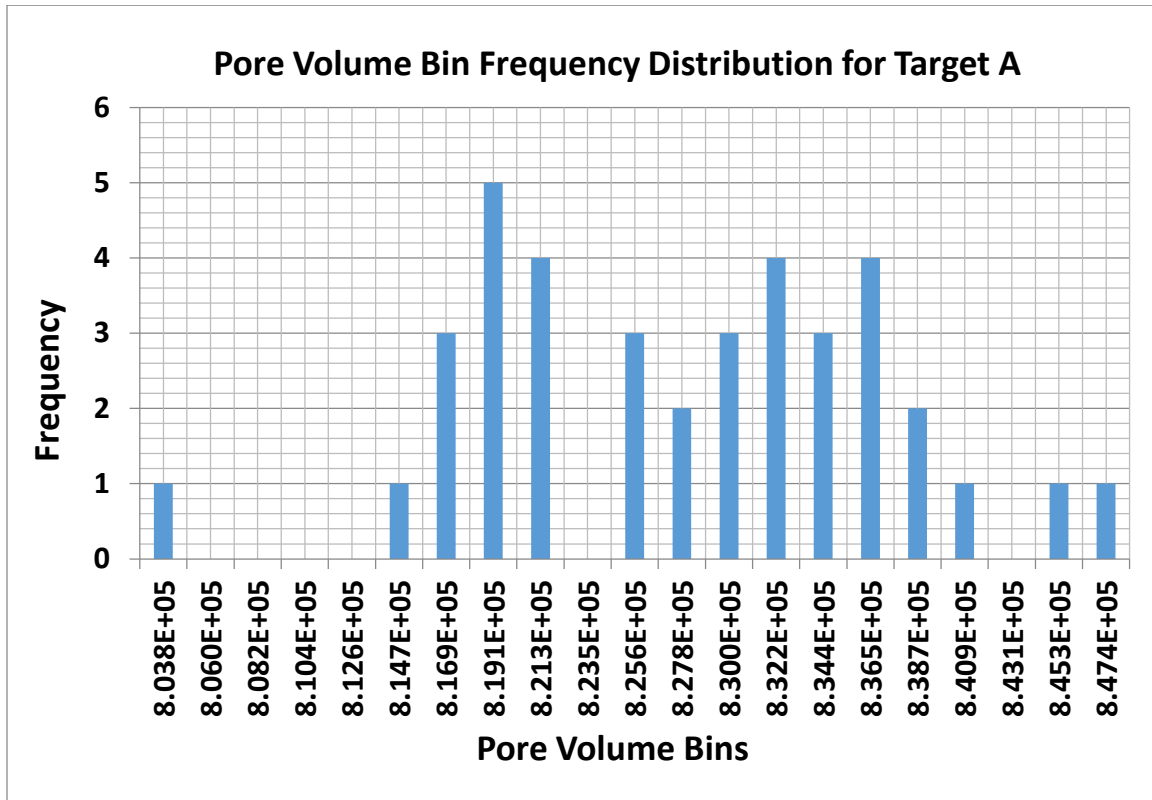


FIG 5. Assigned pore volume bins based on pore volume sum data, plotted with occurrence frequency for the BBRs Formation in a 1 km x 1 km clipped volume centered around the main 10-22 well.

In Figure 6, the P10-50-90 percentiles are labeled on the graph identifying the ranges of data for the PHIE in the BBRs Formation. To obtain the corresponding K_INT volume with respect to the P10-50-90 percentiles, the petrophysical modeling for K_INT was re-run utilizing the collocated co-kriging method. The GRFS algorithm computed the K_INT for the BBRs Formation while using a constant coefficient of 0.7 with respect to each respective P10-50-90 PHIE volume. For each P10-50-90 percentile, there is a corresponding realization number to each. These three realizations of PHIE and corresponding K_INT volumes of the target interval were used in the dynamic fluid-flow simulation for CO₂ injection.

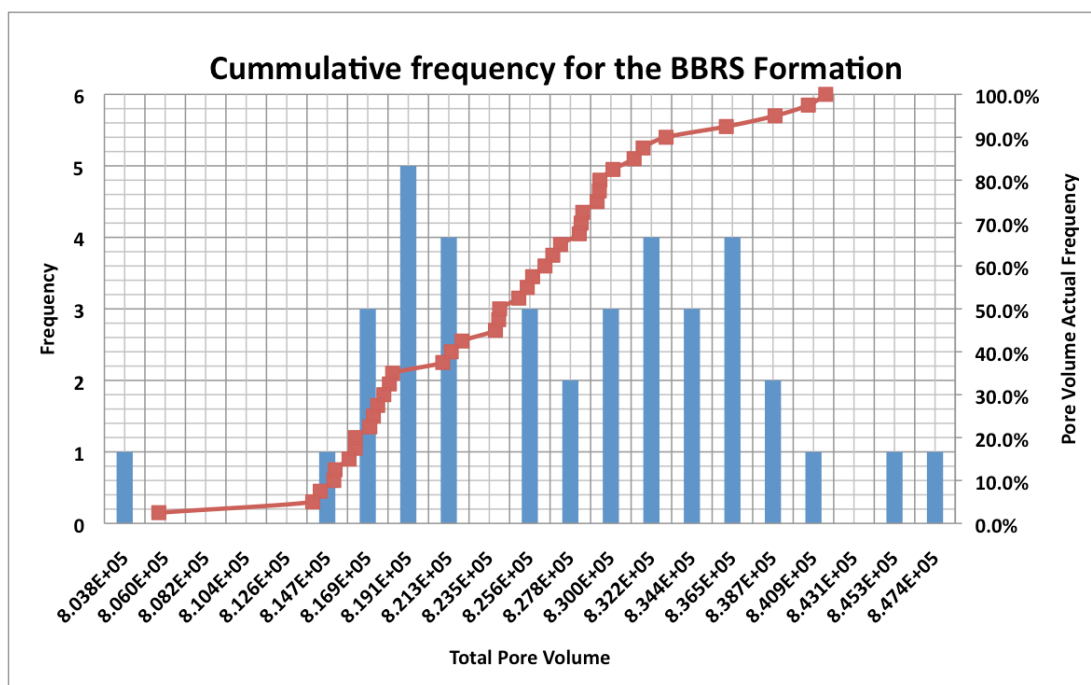


FIG 6. Total effective pore volume data for the BBRs Formation in the 1 km x 1 km clipped volume displaying the occurrence frequency, and the pore volume actual frequency corresponding to the P10-50-90 percentile cases.

Dynamic Fluid-Flow Simulation

Simulation Input Parameters

The primary goal of advancing the static model for dynamic fluid-flow simulations was to obtain a prediction of an injection test for the plume migration and distribution in the BBRs Formation. The dynamic modeling work involves testing of multiple injection scenarios. For the initial model, a single well injection at the 10-22 well located at the center of the model was used with injection rates up to 1000 t/CO₂ per injection over five years.

The 5 km x 5 km model volume with the P10-50-90 PHIE and respective K_{INT} properties was the main input for fluid-flow simulation. The dynamic model was clipped to 4925 m x 4975 m and is composed of the Foremost, BBRs, and Pakowki Formation. Note that these three zones are critical for fluid-flow simulations, as they represent the seal, target, and underlying seal zones. The static model was constructed to have over 60 million 3-D cells, which required the model grid to be upscaled in order for the simulator to utilize the model input. A tartan grid configuration aided in upscaling the model and the number of cells (n) and smallest 3-D cell sizes around the injector well are listed in Table 3. Note the cell size in the Z-direction is listed for the vertical cell heights in the BBRs Formation.

Table 3. Number and size of cells used for upscaling with a Tartan grid configuration.

X		Y		Z	
nX	125	nY	127	nZ	69
Cell size	8.4 m	Cell size	8.4 m	Cell size (BBRS)	0.5 m

From 60 million 3-D cells, the upscaling process decreased this number to just over 1 million 3-D cells in the model (nX , nY , nZ) defined by (125, 127, 69). Figure 7 displays the upscaled tartan grid in plan view of the dynamic geomodel domain. The model grid size was constructed to be 5 km x 5 km, however it is believed with the constant cell sizes in the static model affected the upscaling completed in the dynamic model and resulted in the 4925 m x 4975 m dimensions.

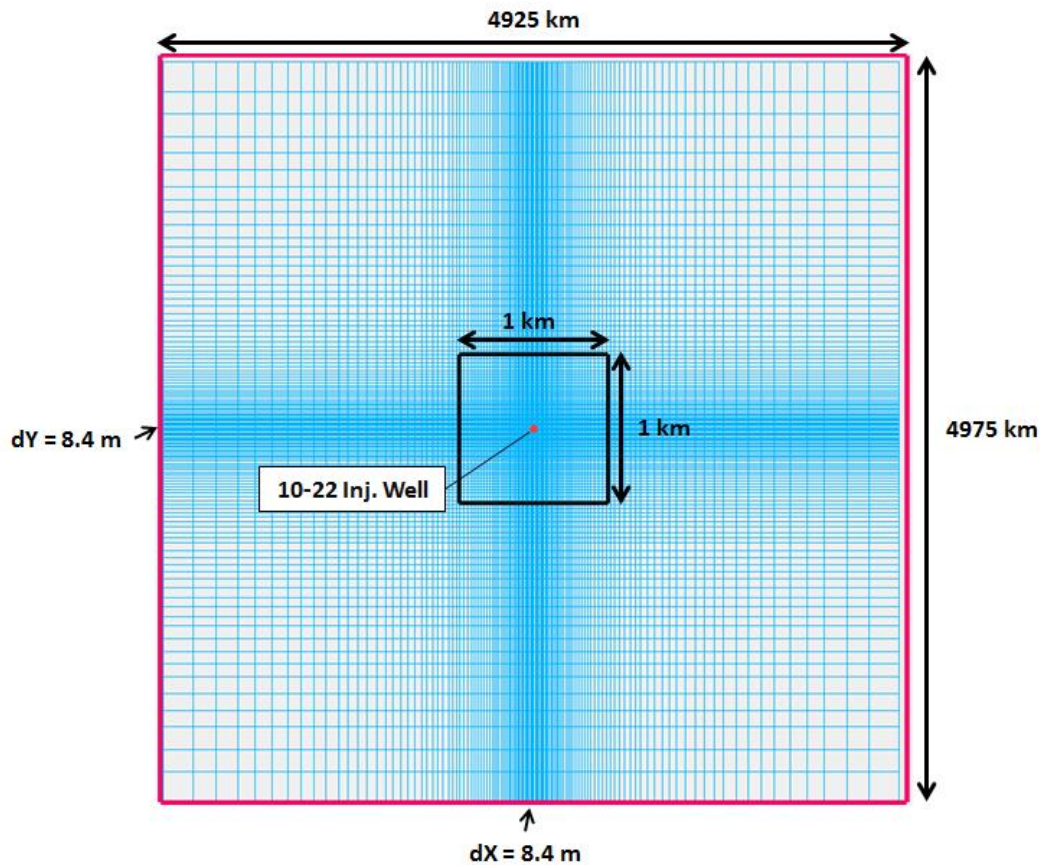


FIG 7. The tartan grid used to upscale the static geomodel. Finer cell sizes (8.4 x 8.4 x 0.5 m) are located closer to the injector 10-22 well. Modified from Lee (2015).

Additional layers in the Z-direction were added at the base of the Foremost Formation to add resolution, and incorporate the lower K_{INT} values within the coal zones directly above the BBRS Formation. The vertical component of cell size plays a critical role to highlight the limiting vertical permeability. With cell sizes too large, the low relative

permeability of the coal zones remains unseen, as it becomes averaged over a larger vertical upscaled cell. Figure 8 demonstrates the thinner layers at the base of the Foremost Formation, directly above the BBRs Formation.

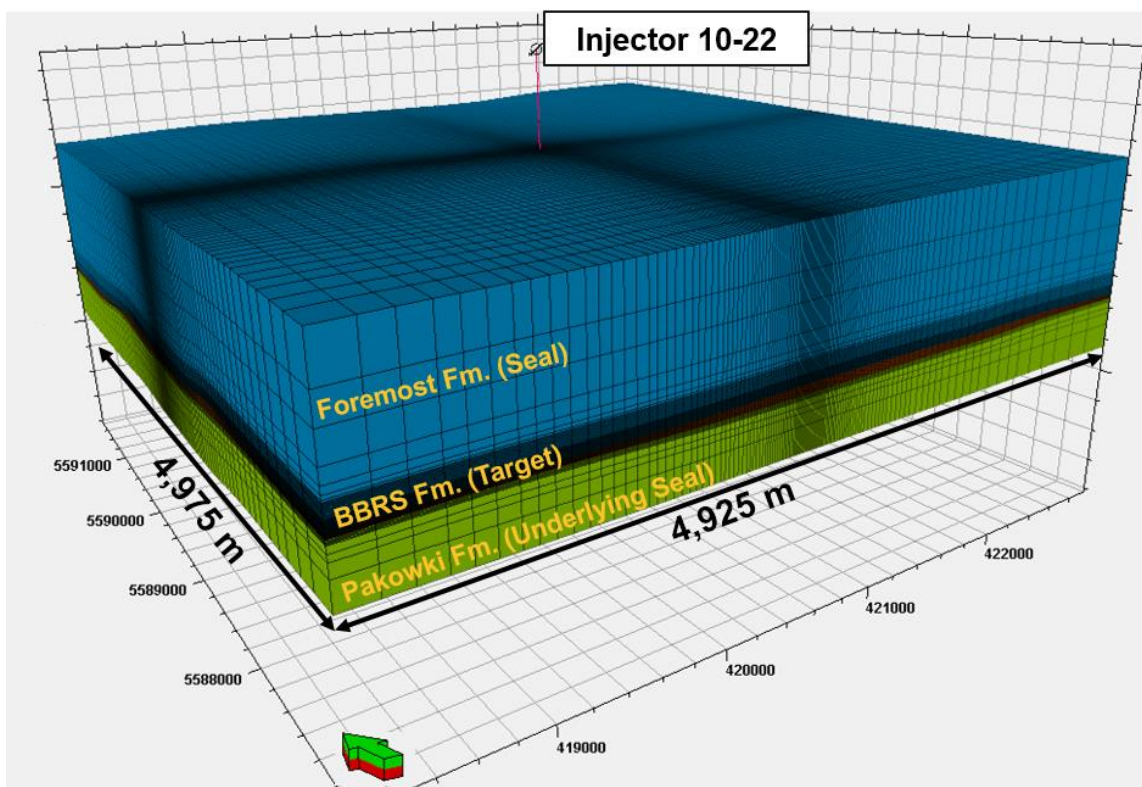


FIG 8. Upscaled 3-D grid of the dynamic model demonstrating the tartan grid configuration used. The three zones consisting of the Foremost, BBRs, and Pakowki Formation are labeled. Figure modified from Lee (2015) with a Vertical Exaggeration (V.E.) of 5.

The reservoir simulation parameters used on the dynamic model are listed in Table 4. The reference datum pressure was estimated using the hydrostatic gradient. The hydrostatic pressure gradient for freshwater is 9.8 kPa/m (Pohl, 2011), thus the pressure at 300 m depth was calculated to be 2.94 MPa. The reservoir temperature was estimated from a single point at target interval depth (300 m) from the Formation Pressure Test (XPT) log. The salinity of formation water is known to be brackish, ranging from 1,000 – 10,000 ppm as determined by a Worley Parsons Komex (2008) report completed in the Newell County region. Rock compressibility was calculated by Goodarzi (2015) using the Geertsma (1957) method. The calculation is based on three core lab measurements within the BBRs Formation that include grain density, bulk density, and total porosity. To avoid pressure build up, pressure breach, or fracturing the reservoir or borehole during injection, the maximum allowable bottom hole pressure (BHP) is a parameter used as a guideline to mitigate this risk. The maximum BHP is considered to be 90% of the lithostatic pressure at reservoir depth needed to fracture the rock. Considering the lithostatic pressure gradient is 24.5 MPa/km (Karner, 2005), at 300 m depth the maximum BHP was calculated to be 6.615 MPa. Of the flow parameters, the ratio of vertical to horizontal intrinsic permeability was estimated to be 1:10, which assumes primary fluids will flow horizontally (Lee, 2015). Injectivity of the reservoir failed to provide useful measurements during a downhole

pressure test conducted in the field of May 2015, and thus was not estimated for parameter input.

Table 4. Reservoir simulation parameters used on the dynamic model for CO₂ injection. Modified from Lee (2015).

Parameter	Value
Pressure (reference datum) at 300 m depth	2.94 MPa
Reservoir temperature (isothermal)	20°C
Salinity	1,000 ppm
Rock compressibility (3 samples near 300 m)	4.18 E-04 (1/bar)
Maximum allowable BHP at 300 m depth	6.615 MPa
k_v/k_h	0.1
CO ₂ -water relative permeability	$S_{wmin}=0.5, k_{rCO2}=0.5$ (end-point gas K_r)

The CO₂-water relative permeability (k_{rCO2}) denoting the irreducible water saturation (S_{wirr}) was estimated using the Brooks-Corey approximation (see Brooks and Corey, 1964; Lee, 2015). This widely accepted model is used for a gas-oil-water system to calculate relative permeability using capillary pressure data (Li and Horne, 2006). From Figure 9 constructed by Lee (2015), the minimum water saturation (S_{wmin}) and critical water saturation (S_{wcr}) are set to 0.5. The maximum water saturation (S_{wmax}) and the water relative permeability at maximum water saturation (k_{rw}) are set to 1. Thus from the graph, when the S_{wmin} is 0.5, the relative permeability of CO₂ to water/brine (k_{rCO2}) is 0.5.

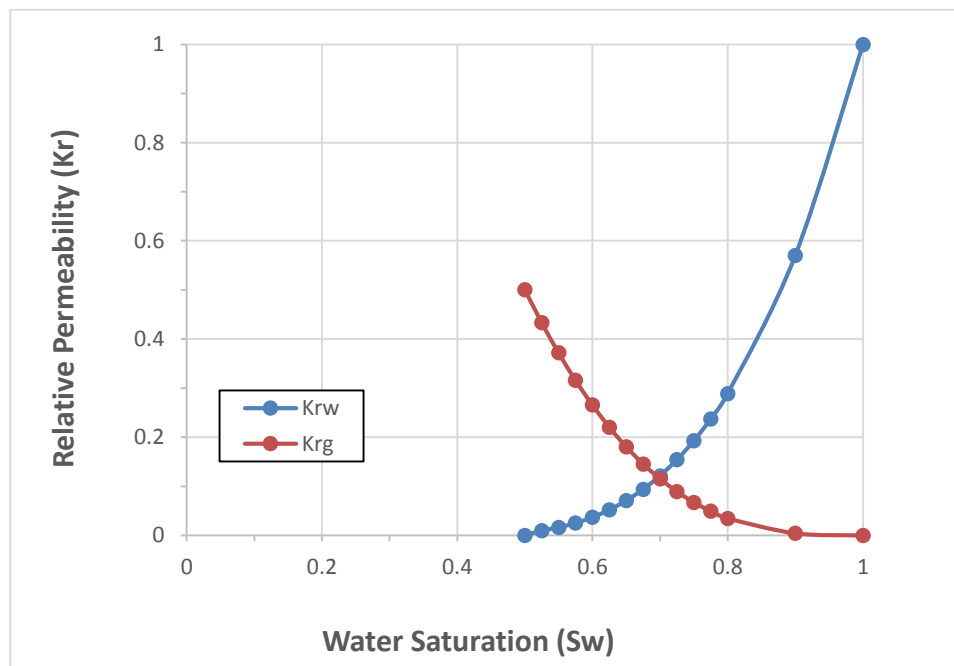


FIG 9. A Brooks-Corey model modification to approximate relative permeability of CO₂ to water saturation.

The inputs for the dynamic model domain include the three geological realizations of PHIE and K_INT that correspond to the approximated P10-50-90 percentiles of the static model data. The dynamic model assumes 100% water saturation and does not consider geochemical or compositional changes of phases. The dynamic model does however consider CO₂ gas dissolution into the formation water in the pore spaces. The initial simulation scenarios intended to have continuous injection period, totaling 1000 t/CO₂ per year over a five-year period. However, the dynamic model parameters are subject to the maximum allowable BHP in the target interval. During the simulation process, the maximum allowable BHP was being exceeded and creating unstable scenarios as the model was unable to reach convergence. The simulation scenarios have been changed to reflect multiple monthly injections with shut-in periods, to allow the formation and borehole pressure to disperse before further injection commences. Table 5 denotes the five-year injection plan used for the three dynamic model simulation scenarios created by Lee (2015).

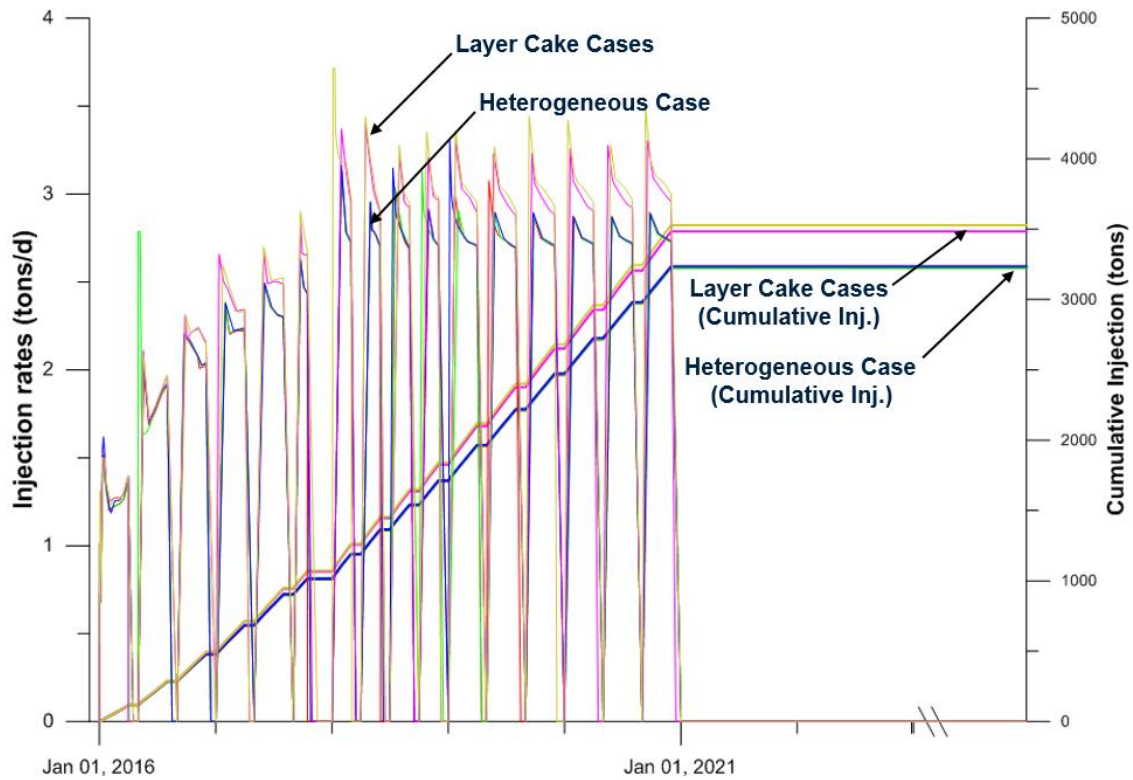
Table 5. Five-year injection plan used for the three dynamic model simulation scenarios.

Date	Injection Period	Shut-in Period
January 1, 2016 – October 14, 2017	3 months	1 month
October 15 – December 31, 2017	-	2.5 months
January 1 – December 31, 2018	2 months	1 month
January 1, 2019 – November 30, 2020	3 months	1 month

Simulation Results

The simulated scenarios for the P10-50-90 case of the 5 km x 5 km geodynamic model are considered to be preliminary findings and are referred to as the heterogeneous case. High levels of uncertainty still remain in the geostatic property model itself, reservoir pressure, fracture pressure, capillary pressure, vertical and horizontal permeability ratio, and the gas-water relative permeability (Lee, 2015).

Another set of 1 km x 1 km layer cake models have been produced and created solely on the basis of the 10-22 well. These two layer cake models also have P10-50-90 scenarios for PHIE and K_INT. The average permeability amongst the three models appears to change. A higher average K_INT in the BBRs Formation in the P50 case of 0.62 mD was found for the layer cake models, in comparison to the 0.47 mD of the larger heterogeneous case. The layer cake models lack complexity, and assume a single connectivity where an entire subsurface layer is assigned a K_INT value without changing from cell to cell. Whereas the heterogeneous case changes from cell to cell, and has various K_INT inputs from surrounding wells as assigned by the zones variogram values. Figure 10 displays the dynamic simulation results for the injected CO₂ into the BBRs Formation for the full lifetime period of the project.



Legend

Inj Rate, P90	Cumulative Inj, P90
Inj Rate, P50	Cumulative Inj, P50
Inj Rate, P10	Cumulative Inj, P10
Inj Rate, Layer Cake w/ Structural Variations	Cumulative Inj, Layer Cake w/ Structural Variations
Inj Rate, Layer Cake	Cumulative Inj, Layer Cake

FIG 10. Simulated CO₂ injection into the BBRs Formation over a five-year period constrained by the maximum allowable BHP. Figure taken by Lee (2015).

The higher average K_{INT} values in the layer cake cases demonstrate increased injection rates, leading to a greater overall cumulative injection of CO₂ into the target interval. The gap space between the monthly injections are represented as the shut-in periods, where injection ceases to allow the formation pressure to dissipate and the plume to move away from the borehole. The shape of the graph during injection period is representative of a pressure differential (Δp) in the reservoir. After a shut-in period, the pressure of the reservoir is lowered. The next injection period then experiences a Δp , with low formation pressure and then high pressures from the injection of CO₂. As observed from the graph, the higher the Δp allows for greater injectivity rates of CO₂ and are marked by the peaks at the beginning of each monthly injection period. As injection proceeds, the Δp decreases as a result of the formation pressure rising and is depicted by the decreasing injection rates that follow the initial peak of the monthly injection period. For the

heterogeneous and layer cake models, the P90 case for displays higher injection rates than the P50 case, which is always greater than the P10 case.

The injection rates for both the heterogeneous and layer cake models appear to gradually increase over time and reach a plateau. This is caused by the CO₂ gas-water saturation effect or the relative permeability hysteresis, where the k_{rCO_2} increases over time as a result of the decreasing water saturation. Initially, the simulation scenarios begin with a S_w of 1 and a CO₂ gas saturation (S_{CO_2}) of zero as injection has not commenced. Comparing initial injection periods to later periods of injection, the injection rates of CO₂ appear to increase. For example, from Figure 10 the initial injection rate begins at 1.5 ton/day and increases to just over 3 tons/day over two years. Typically, “the relative permeability for a given phase is greater when its saturation is being increased rather than decreased” (Bennion et al., 1996). The increased injectivity is demonstrating this effect, where greater CO₂ saturations increased the k_{rCO_2} . Another factor to consider is that gas compressibility is much greater than formation water. As well, the CO₂ gas is compositionally changing the system as it dissolves into the formation water. The simulated scenarios do not take into account further complexity of reservoir changes, such as chemical dissolution or precipitation of minerals within the rock. For all P10-50-90 cases, the injectivity remains steady after a period of time, depicting greater CO₂ saturation levels in the BBRs Formation. This plateau also represents the formation reaching the 90% of lithostatic pressure, as to not fracture the reservoir and maintain integrity for both the target and seal intervals. Following the plateau of increased injection rates per day, the simulated monthly CO₂ injections cease. A ten-year post-injection period is modeled to determine the saturation percentage of CO₂ in the target and seal intervals. Further results for the layer cake cases will not be discussed, and further simulation results reported focus on the 5 km x 5 km heterogeneous case.

Amongst the three P10-50-90 PHIE and K_INT cases, there were no significant variations in the simulation results for the heterogeneous geodynamic model. The 3-D cross-sectional view of the plume distribution for one year into injection period for the P50 case appears to be asymmetrical, and is shown in Figure 11. The plume shape is mainly driven by the k_v/k_h ratio and buoyancy of the system. The injected CO₂ plume appears to be mainly contained within the BBRs Formation, and extends approximately 50 m away from the 10-22 injector well. The CO₂ gas saturation remains the highest near the well at 0.45 and dissipates outwards to 0.30.

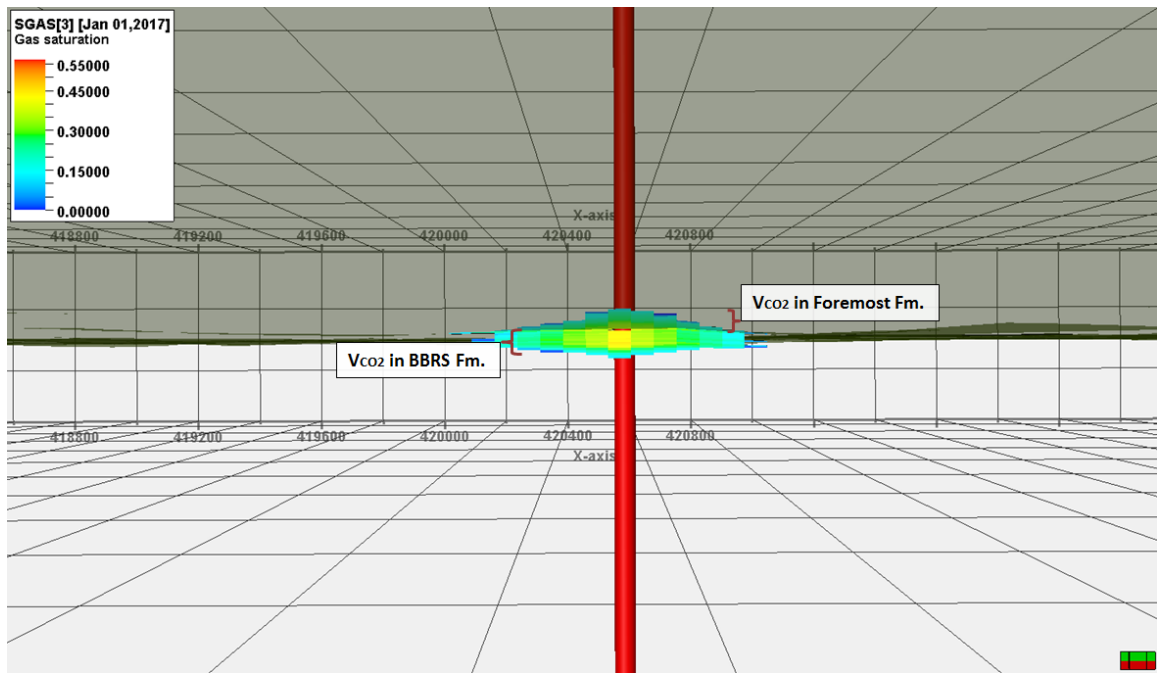


FIG 11. 3-D cross-section displaying the distribution of the injected CO₂ plume one year into the injection period for the P50 case in the heterogeneous geodynamic model with V.E. of 1.

The 3-D plume distribution for five years into injection period for the P50 case is shown in Figure 12. The plume displays a greater horizontal distribution, as it expands laterally into the BBRs Formation. The injected CO₂ plume appears to still be mainly contained within the BBRs Formation, with minor vertical migration of approximately 10 m into the Foremost Formation. The CO₂ gas saturation radially decreases away from the well, remaining the highest at 0.50 near the injector and decreases to 0.40 at approximately 50 m and down to 0.20 at 100 m from the well.

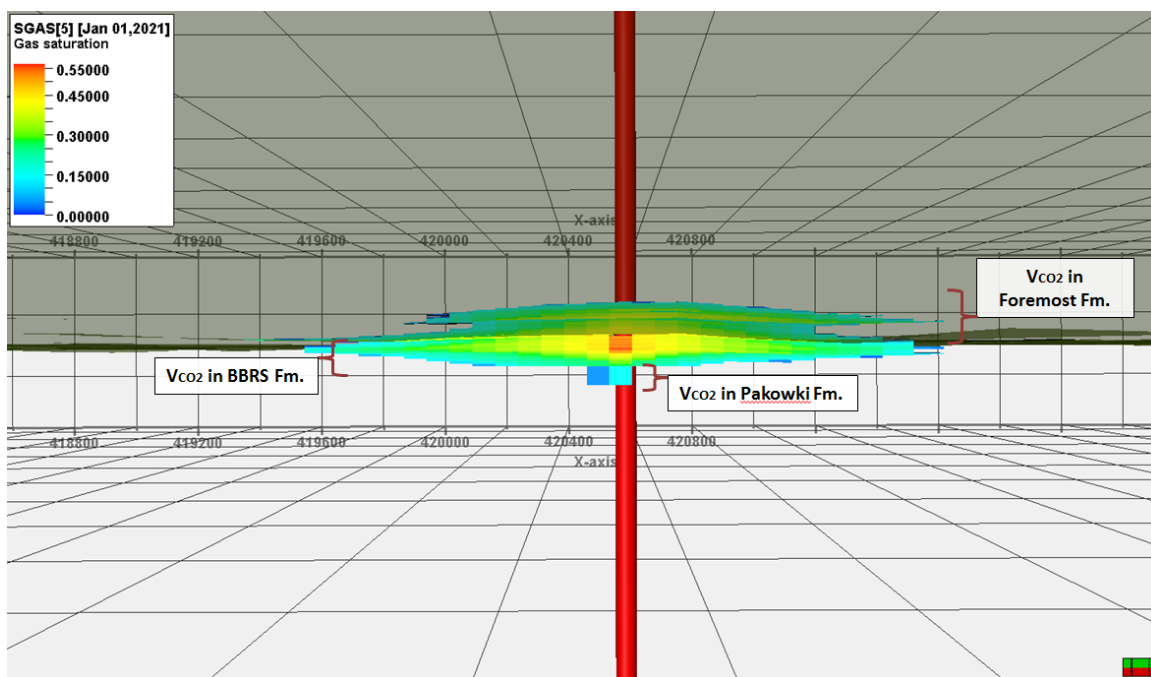


FIG 12. 3-D cross-section displaying the distribution of the injected CO₂ plume five years into the injection period for the P50 case in the heterogeneous geodynamic model with V.E. of 1.

The 3-D plume distribution for the 1-year post-injection period for the P50 case is shown in Figure 13. The plume is laterally extensive, as it has expanded and saturated the BBRS Formation but also demonstrates a greater volume of CO₂ that has migrated vertically into the Foremost Formation. The top of the plume displays a flat appearance, which is interpreted to be caused by the impermeable coal zone. The coal zone is disabling further vertical migration, and causing the plume to distribute itself laterally to account for the CO₂ volume. The vertical extent of the CO₂ plume that has moved into the seal is estimated at 15 m. The plume edge remains extended at approximately 125 m away from the 10-22 injector well in the E-W direction. Similarly to the plume evolution during the injection period, the CO₂ gas saturation radially decreases away from the well. The highest CO₂ gas saturation at the 10-22 well is 0.50, and decreases to 0.40 at approximately 50 m, and decreases further to 0.20 at 100 m from the well.

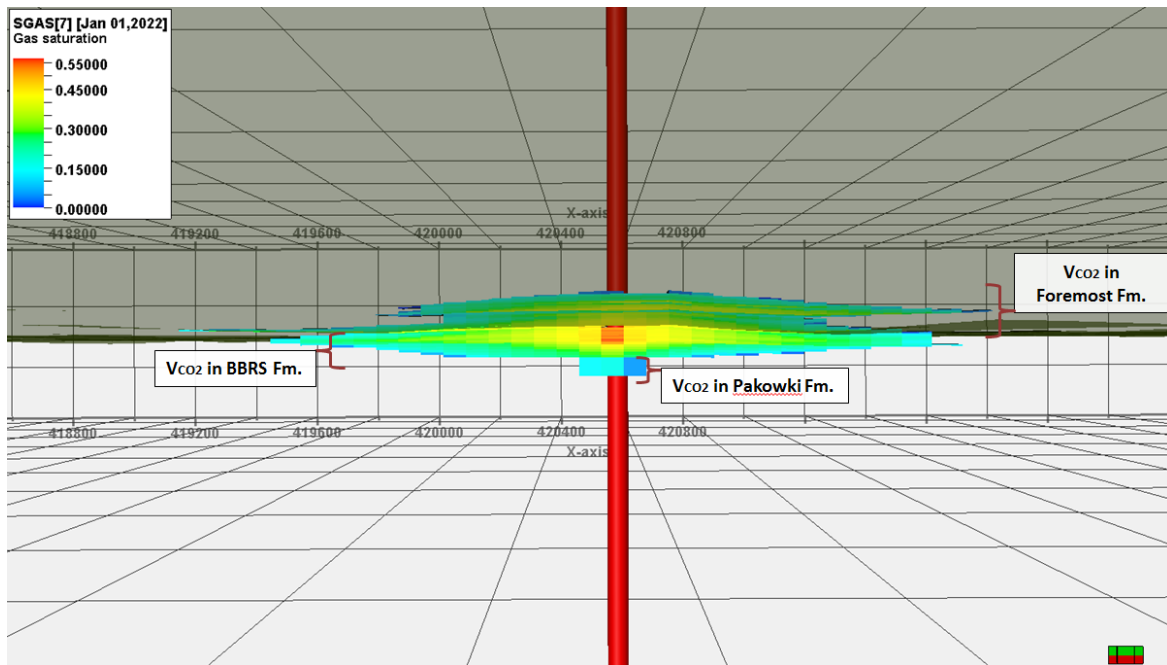


FIG 13. 3-D cross-section display of the distribution of the injected CO₂ plume 1 year post-injection for the P50 case in the heterogeneous geodynamic model with V.E. of 1.

The 3-D plume distribution for the 10-year post-injection period for the P50 case is shown in Figure 14. The plume has vastly extended laterally both in the BBRs and Foremost Formation, reaching approximately 175 m away from the 10-22 well in the E-W direction and totaling a 350 m plume in length. Building from the 1-year post-injection simulation results, a greater volume of CO₂ has migrated vertically into the Foremost Formation reaching a total of 20 m from the top of the BBRs Formation. The top of the plume continues to display a flat appearance, with minor coning as a result of buoyancy. Over 10-years, CO₂ gas saturation remains similar to the 1-year post injection simulation results in that the highest CO₂ gas saturation occurs at the 10-22 injector well in the BBRs Formation. The gas saturation decreases radially away from the well, where the highest CO₂ gas saturation is 0.50, decreasing to 0.40 at approximately 20 m, 0.35 to 0.30 at a distance of 80 m away, and down to 0.20 at over 100 m away from the injector well. The gas saturation behaves similarly in the vertical direction, where 0.50 remains at a distance of 10 m, dissipating to 0.20 over a shorter distance as a result of the low k_v/k_h ratio of 0.1.

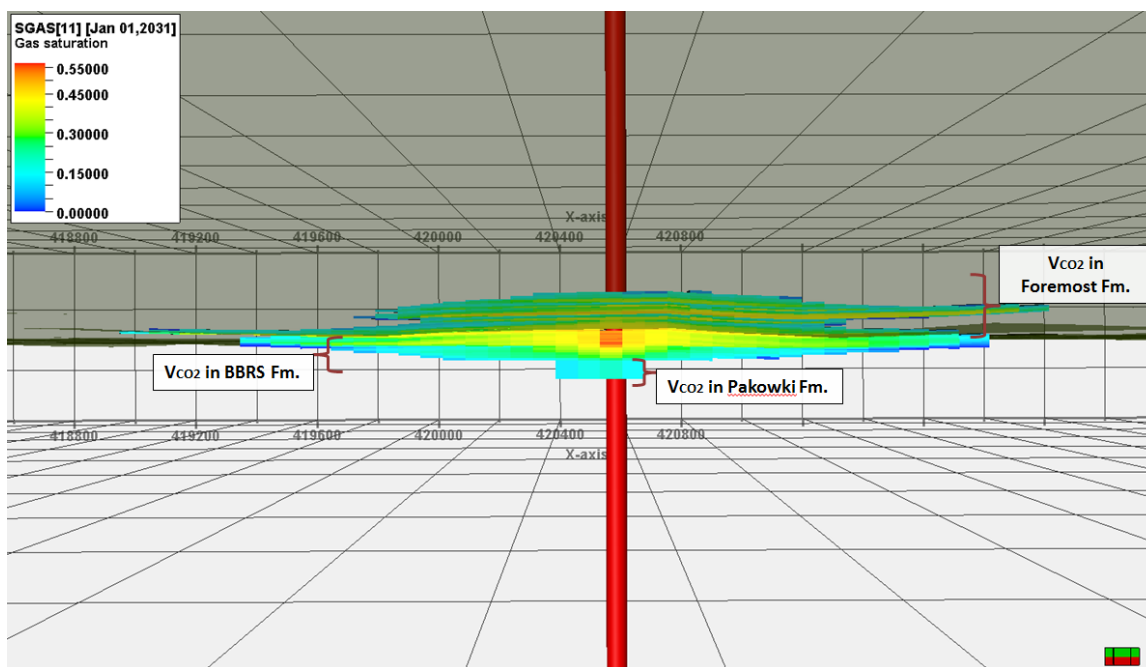


FIG 14. 3-D cross-section display of the distribution of the injected CO₂ plume 10 years post-injection for the P50 case in the heterogeneous geodynamic model with V.E. of 1.

The four cases described above can be more easily observed in 2-D (Figure 15), where screen captures of the simulated scenarios were taken in the Eclipse software by Lee (2015). The CO₂ gas saturation profile is displayed in the E-W direction for the (A) 1-year during injection, (B) 5-years during injection, (C) 1-year post-injection, and (D) 10-years post-injection periods.

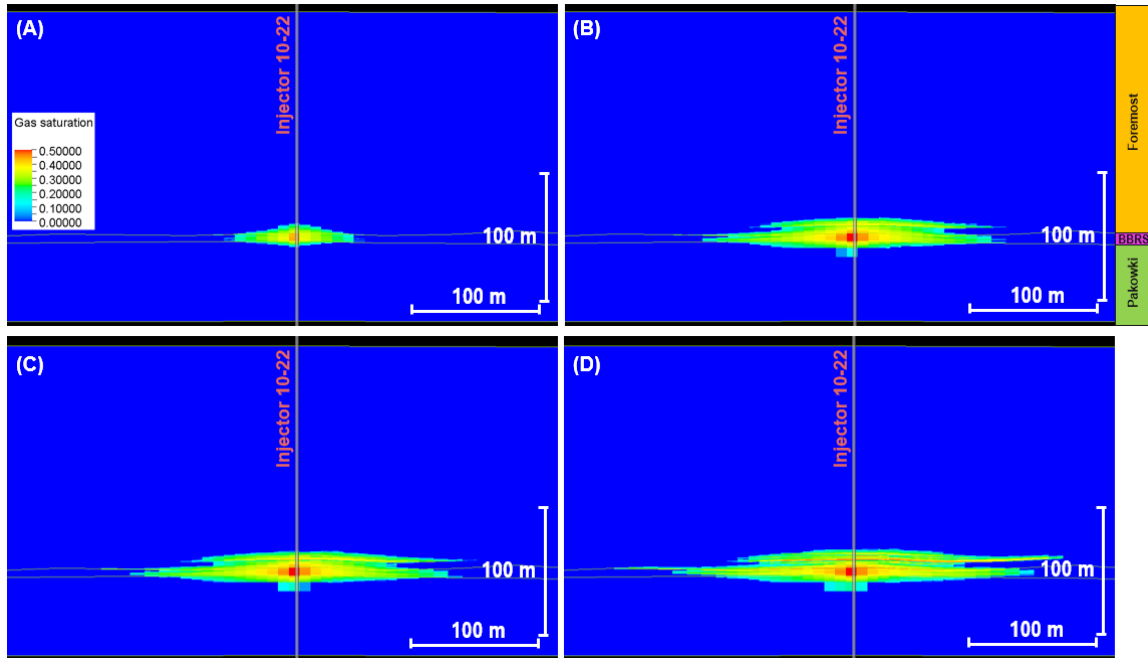


FIG 15. CO₂ saturation profile along the E-W direction for the P50 case of the heterogeneous model. (A) After 1-year during the injection period, (B) after 5-years during the injection period, (C) 1-year post-injection period, and (D) 10-years post-injection period. Figures taken by Lee (2015).

The lateral and vertical extent of the CO₂ plume from the preliminary simulated scenarios does not show immediate concern for the plume rising to the exposed Earth surface. The 5 km x 5 km heterogeneous geodynamic model including input from 88 wells was able to contain the CO₂ plume within 175 m from the 10-22 well. Looking at the plume distribution from above (Figure 16), the evolution consistently demonstrated a radially enlarged diamond-shaped plume. It is believed that the diamond-shape plume is an artifact of the tartan gridding used to upscale the static geomodel (Lee, 2015). To reduce this effect, further work has been completed on the layer cake cases to utilize constant cell sizing.

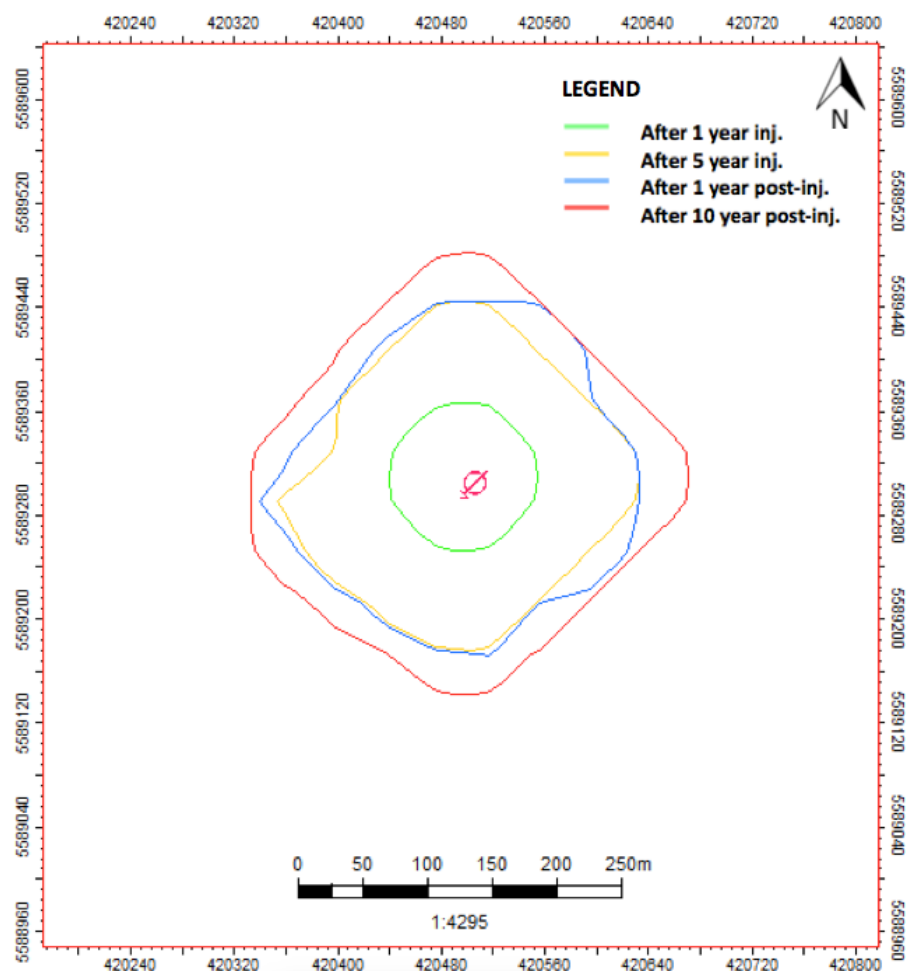


FIG 16. Plan view of the simulated scenarios for the P50 case of the heterogeneous model, depicting the CO₂ plume edges. Modified from Lee (2015).

The dynamic simulation results of the geomodel conclude containment of the total injection of 5000 t of CO₂ over a five-year intermittent period. The P10-50-90 K_INT and PHIE properties show minimal change of the plume distribution and injection rates between the three cases. The BBRs Formation as the target interval appears to be an ideal reservoir with good porosity, but a target with greater permeability would allow for greater injectivity. The Foremost Formation as a seal is very unique, with numerous interbedded zones varying from siltstone, shale, sandstones to coal. The coal zone that lays directly above the target interval, known as the McKay coal zone, appears to support the integrity of the seal interval. The low relative permeability values and effective porosity prove to hinder vertical migration of the CO₂ plume.

After 1-year post-injection, the simulated plume is laterally extensive and expands to a total length of 250 m in the E-W direction and reaches 15 m above the BBRs Formation. A CO₂ plume of this size should be able to be detected with basic MMV technologies, such as the downhole logging suite, pressure monitoring, chemical tracers, microseismic, and 4-D time lapse reflection seismology. Further simulation scenarios will be tested on the layer cake models and analyzed, in order to account for the volume of uncertainties that exist in both the geostatic and geodynamic models. Both models at the layer cake and

heterogeneous scale can be improved with larger volumes of higher quality field data measurements. These heterogeneous simulation results mark the preliminary commencement of moving towards obtaining an injection license, and have proved to be an educational experience. Recalling on the principles of uncertainty, model complexity does not prove to add or take away accuracy but knowledge of both static and dynamic uncertainty sources does.

SUMMARY AND FUTURE WORK

The developed 5 km x 5 km static geomodel was further characterized with receipt of newer data inputs. The total and effective porosity were calculated by using a volume of clay approach, separating the free- and bound fluids in the formation pore spaces. The intrinsic permeability was calculated using the free-fluid Timur-Coates model. Both effective porosity and intrinsic permeability were calibrated to six core lab measurements. A relationship between the core measurements and calculated wireline logs was established to propagate these properties through the entire model extent. The model workflow was then rerun, where properties were upscaled and populated into the 3-D cells using a Gaussian Function Simulation Algorithm.

To gain a better understanding of the uncertainty within the data, a P10-50-90 framework was adopted to characterize the conservative, typical, and optimistic ranges of the effective porosity and intrinsic permeability in the seal and target injection intervals. The static geomodel input was upscaled using a tartan gridding system to reduce the number of 3-D cells. Model input parameters including maximum allowable BHP, salinity, rock compressibility, water saturation, and CO₂-water relative permeability were calculated and used for the dynamic fluid-flow simulations. To mitigate exceeding maximum allowable BHP, multiple monthly injection scenarios with shut-in periods was simulated over a five-year period. Dynamic simulation was completed on the P10-50-90 static cases for multiple injection scenarios, totaling 1000 t/CO₂, per year for a five-year period. There were no significantly noted variations in the simulation results between the three static cases. The evolution of the CO₂ plume was observed at 1-year during injection and 5-years during injection, as well as the 1-year and 10-year mark for the post-injection period. The final 10-year post-injection result simulated a laterally extensive plume, expanding to 350 m in length and 20 m of vertical migration above the BBRS Formation.

The thin target interval proves to be an ideal reservoir, and the seal interval demonstrates containment and conformance over a 10-year post-injection period. Static and dynamic uncertainties remain in estimating the reservoir pressure, fracture pressure, capillary pressure, as well as the gas-water relative permeability. Further work is being completed on a 1 km x 1 km layer cake case, and will be used as documentation as a step towards obtaining the injection license as part of Directive 051 from the Alberta Energy Regulator.

ACKNOWLEDGEMENTS

We thank Lee Swager (Petrophysicist – Schlumberger Ltd. Denver), Wade Zaluski (Geomodeler – Schlumberger Canada Ltd.), and Si-Yong Lee (Reservoir Engineer – Schlumberger Ltd. Denver). This extreme-team trio have contributed to the project by providing extensive expertise, conceptual discussions, and a breadth of knowledge in petrophysics, static modeling, and dynamic modeling, respectively.

Thank you to CMC Research Institutes, Inc. for providing the funding for this research to develop the Field Research Site (FRS) in Alberta. We would also like to thank CREWES industrial sponsors and NSERC (Natural Science and Engineering Research Council of Canada) through the grant CRDPJ 461179-13 for supporting JD's academic pursuits.

Thank you to CREWES staff and students, especially Roy Lindensmith for his suggestions, assistance with proof-reading, and invaluable discussions.

Thank you to Schlumberger Canada Limited for providing the Petrel™ E&P Software Platform, whose license was provided to the Department of Geoscience at the University of Calgary and was used for the development of the geostatic model.

Lastly, thank you to IHS Energy Canada for providing Accumap® and Acculog® software, whose license was provided to the Department of Geoscience at the University of Calgary and was used to obtain the extensive well data used in this project.

REFERENCES

- Allen, D., Bedford, J., Castelijns, K., Fairhurst, D., Gubelin, G., Heaton, N., Minh, C.C., Norville, M.A., Seim, M.R., Pritchard, T., and Ramamoorthy, R. (2000). Trends in NMR Logging. *Oilfield Review*, Autumn 2000. Obtained October 22, 2015 from https://www.slb.com/~media/Files/resources/oilfield_review/ors00/aut00/p2_19.pdf.
- Beaton, A. (2003). Coal-Bearing Formations and Coalbed-Methane Potential in the Alberta Plains and Foothills. Alberta Energy and Utilities Board/Alberta Geological Survey. CSEG Recorder, vol. 28(9). Obtained on October 19, 2014 from <http://csegrecorder.com/articles/view/coal-bearing-formations-and-coalbed-methane-potential-in-the-alberta-plains>.
- Bennion, D.B., Thomas, F.B., and Bietz, R.F. (1996). Hysteretic Relative Permeability Effects and Reservoir Conformance – An Overview. Hycal Energy Research Laboratories Ltd. Pp. 1-7.
- Bentley, M. (2013). Modelling for Comfort. AGR TRACS Training. Capturing Uncertainty in Geomodels: Best Practices and Pitfalls. Abstract Book, December 11-12, 2013.
- Bond, C.E. (2013). Methods to Minimize and Capture Uncertainty during Model Creation. Capturing Uncertainty in Geomodels: Best Practices and Pitfalls. Abstract Book, December 11-12, 2013. Geology and Petroleum Geology, Kings College, University of Aberdeen, AB24 3UE.
- Brooks, R.H. and Corey, T. (1964). Hydraulic Properties of Porous Media. *Hydrology Papers*, vol. 3, Colorado State University, Fort Collins, Colorado.
- Coates, G.R. and Dumanoir, J.L. (1974). A new approach to improved log-derived permeability. *The Log Analyst*, pp. 17.
- Cox, D.J., Cottam, M.A., Carruthers, R.A., Laws, E., and Nash, T. (2013). Capturing Stratigraphic and Depositional Framework Uncertainty in Inter-Well Areas: An Example from the Magnus Field, Northern North Sea, UK. Capturing Uncertainty in Geomodels: Best Practices and Pitfalls. Abstract Book, December 11-12, 2013. BP Exploration Operating Company Limited, 1-4 Wellheads Avenue, Dyce, Aberdeen, AB21 7PB.
- Dongas, J.M. and Lawton, D.C. (2014). Development of a geostatic model for a geoscience field research station in Alberta: CREWES Research Report, **26**, Chapter 22, pp. 1-47.

- Fichtl, P., Hirst, P., and Kaesbach, I. (2013). From subsurface uncertainty assessment to risk management: How to make best use of our static reservoir models. *Capturing Uncertainty in Geomodels: Best Practices and Pitfalls*. Abstract Book, December 11-12, 2013. BP Exploration Operating Company Limited, Chertsey Road, Sunbury-on-Thames, TW16 7LN.
- Gardiner, S., Thomas, D.V., Bowering, E.D., and McMinn, L.S. (1990). *A Braided Fluvial Reservoir, Peco Field, Alberta, Canada*. Casebooks in Earth Science Sandstone Petroleum Reservoirs, New York, New York: Springer-Verlag New York Inc, Pp. 45-46.
- Geertsma, J. (1957). The effect of fluid pressure decline on volumetric changes of porous rock. Society of Petroleum Engineers, published in *Petroleum Transactions, AIME*, vol. 210, pp. 331-340.
- Goodarzi, S. (2015). Personal Communication. Reservoir-Geomechanics Engineer, Taurus Reservoir Solutions Ltd., 1015-4th Street SW, Calgary, Alberta, T2R 1J4.
- Hamblin, A.P. and Abrahamson, B. (1993). Offlapping progradational cycles and gas pool distribution in the Upper Cretaceous “Basal Belly River” sandstones, Judith River Group, Southern and Central Alberta. Geological Survey of Canada, Natural Resources Canada, Open File 2672, Pp. 10.
- Herron, M.M. (1987). Estimating the Intrinsic Permeability of Clastic Sediments from Geochemical Data. Society of Petrophysicists and Well-Log Analysts, Twenty-Eighth Annual Logging Symposium. Pp. 1-23.
- Höcker, C. (2013). Structural uncertainty – Real or caused by flaws in analysis and modeling? *Capturing Independent geoscience advisor, consulting with Nexen Petroleum U.K. and Baker Hughes*. *Uncertainty in Geomodels: Best Practices and Pitfalls*. Abstract Book, December 11-12, 2013.
- Karner, S.L. (2005). Stimulation techniques used in enhanced geothermal systems: Perspectives from geomechanics and rock physics. Stanford Geothermal Workshop, HDR/EGS Session, Stanford University, Stanford, California, SGP-TR-176.<http://www.geothermal-energy.org/pdf/IGAstandard/SGW/2005/karner.pdf>.
- Lee, S.Y. (2014-5). Personal Communication. Reservoir Engineer, Carbon Services. Schlumberger Canada Limited, 200 125-9th Avenue SE, Calgary, Alberta, T2G0P6.
- Li, K. and Horne, R.N. (2006). Comparison of methods to calculate relative permeability from capillary pressure in consolidated water-wet porous media. *American Geophysical Union, Water Resources Research*, vol. 42, W06405, DOI: 10.29/2005WR004482.
- Luthi, S.M. (2013). *Geological Well Logs: Their use in reservoir modeling*. Springer Science & Business Media. Pp. 178.
- Mao-Jones, J. (2012). *Decision & Risk Analysis*. The Merrick Consultancy. Obtained April 16, 2014 from <http://www.merrick.com/merrickandcompany/media/Resources/Energy/Whitepapers/Merrick-Decision-Risk-Analysis-White-Paper.pdf?ext=.pdf>.
- Meunier, R., Chautru, J.M., Jeannée, N. (2013). Model-derived uncertainties or uncertainty about models? Geovariances, France. *Capturing Uncertainty in Geomodels: Best Practices and Pitfalls*. Abstract Book, December 11-12, 2013.
- Meurant, G. (2011). Belly River Pool, Pembina Oil Field, Alberta. *Geomorphology of oil and gas fields in sandstone bodies*. *Developments in Petroleum Science 4*. Amsterdam, The Netherlands: Elsevier Scientific Publishing Company, Pp. 129-131.
- Meyers, R. (2014). *Petrophysical Techniques*. Permeability lecture notes. University of Calgary, Department of Geoscience.

- Nolen-Hoeksema, R. (2014). Flow Through Pores. *Oilfield Review* 2014, vol. 26(3). Obtained October 22, 2015 from http://www.slb.com/news/inside_news/2015/~media/Files/resources/oilfield_review/ors14/aut14/define_perm.ashx.
- Oxford Instruments Industrial Analysis. (2014). NMR log calibration from laboratory core measurements. *GeoSpec Application Note 3*. Obtained October 23, 2015 from <http://www.oxford-instruments.com/OxfordInstruments/media/industrial-analysis/magnetic-resonance-pdfs/GeoSpec-App-Note-NMR-Log-Calibration.pdf?width=0&height=0&ext=.pdf>.
- Pedersen, P.K. (2013-4). Personal Communication. Associate Professor, Department of Geoscience. University of Calgary, 2500 University Dr. NW, Calgary, Alberta, T2N 1N4.
- Petrowiki. (2015). Permeability Determination. Obtained October 23, 2015 from http://petrowiki.org/Permeability_determination.
- Pohl, W.L. (2011). Chapter 7: Petroleum and Natural Gas Deposits. *Economic Geology: Principles and Practice*. West Sussex, UK: John Wiley and Sons Ltd. Pp. 561.
- Rider, M. and Kennedy, M. (2011). *The Geological Interpretation of Well Logs*. 3rd Edition, published by Rider-French Consulting Ltd. Pp.132.
- Rushing, J.A., Newsham, K.E., Lasswell, P.M., Cox, J.C., and Blasingame, T.A. (2004). Klinkenberg-Corrected Permeability Measurements in Tight Gas Sands: Steady-State Versus Unsteady-State Techniques. *Society of Petroleum Engineers Inc*, 89867, pp. 1-11.
- Schlumberger Inc. (2015). *Petrel E&P Platform Help File*. License used in the Department of Geosciences, University of Calgary, 844 Campus Place NW, Calgary, Alberta, T2N 1N4.
- Schlumberger Oilfield Glossary. (2015). Porosity. Obtained October 21, 2015 from http://www.glossary.oilfield.slb.com/en/Terms/u/unsteady_state.aspx.
- Schlumberger Oilfield Glossary. (2015). Unsteady State. Obtained October 22, 2015 from http://www.glossary.oilfield.slb.com/en/Terms/u/unsteady_state.aspx.
- Schlumberger Reservoir Laboratories Canada. (2015). *Final Core Analysis Report*. Prepared for CMC Research Institutes, Inc for Countess 10-22-17-16W4, License: AB0474436, SRL Project Number: 20150033, August 2015.
- Skinner, G. (2013). Wellbore position uncertainty: a primer for Geomodellers. Baker Hughes. *Capturing Uncertainty in Geomodels: Best Practices and Pitfalls*. Abstract Book, December 11-12, 2013.
- Skorstad, A. and Leahy, G. (2013). Propagating Uncertainties through Disciplines – Avoiding Local Optimizations on Wrong Assumptions. Roxar Software Solutions. *Capturing Uncertainty in Geomodels: Best Practices and Pitfalls*. Abstract Book, December 11-12, 2013.
- Stunell, M. (2013). Integration Matters – The challenge of adopting technology for effective subsurface uncertainty assessments. Reservoir Engineering Technical Consultant, Schlumberger Information Solutions. *Capturing Uncertainty in Geomodels: Best Practices and Pitfalls*. Abstract Book, December 11-12, 2013.
- Swager, L. (2014-5). Personal Communication. Senior Petrophysicist, Carbon Services. Schlumberger Limited, 1875 Lawrence St Ste 500, Denver, CO 80202.
- Tanikawa, W. and Shimamoto, T. (2006). Klinkenberg effect for gas permeability and its comparison to water permeability for porous sedimentary rocks. *Hydrology and Earth System Sciences Discussions*, 3, pp. 1315-1338. <http://www.hydrol-earth-syst-sci-discuss.net/3/1315/2006/hessd-3->

1315-2006-print.pdf.

Thomas, L. (2002). *Coal Geology*. John Wiley & Sons. Obtained online on April 16, 2014 from http://books.google.ca/books?id=4oYWx90ybY8C&printsec=frontcover&source=gbs_ge_summar_y_r&cad=0#v=onepage&q&f=false.

Timur, A. (1968). An investigation of permeability, porosity, and residual water saturation relationship for sandstone reservoirs. *The Log Analyst*, vol. 9(4), pp. 8.

WorleyParsons Komex. (2008). *Regional Groundwater Resource Assessment for the County of Newell No. 4. Resources and Energy, Environment & Water Resources*. County of Newell and AAFC-PFRA, pp. 1-105.

Zaluski, W. (2014-5). Personal Communication. Senior Geologist, Carbon Services. Schlumberger Canada Limited, 200 125-9th Avenue SE, Calgary, Alberta, T2G0P6.